

Numerical Analysis of The Ti6Al4V Behavior Based on the Definition of a New Phenomenological Model

Mariem YAICH (✉ yaichmariem@gmail.com)

Arts et Métiers ParisTech, LAMPA, 2 bd du Ronceray, 49035 Angers CEDEX

Yessine Ayed

Arts et Métiers ParisTech, LAMPA, 2 bd du Ronceray, 49035 Angers CEDEX

Guenael Germain

Arts et Métiers ParisTech, LAMPA, 2 bd du Ronceray, 49035 Angers CEDEX

Zoubair Bouaziz

Université de Sfax, Ecole Nationale d'Ingénieurs de Sfax

Research Article

Keywords: Ti6Al4V, VUMAT, Constitutive model, Chip segmentation, Orthogonal machining

Posted Date: May 5th, 2021

DOI: <https://doi.org/10.21203/rs.3.rs-433009/v1>

License: © ⓘ This work is licensed under a Creative Commons Attribution 4.0 International License.

[Read Full License](#)

Version of Record: A version of this preprint was published at The International Journal of Advanced Manufacturing Technology on July 24th, 2021. See the published version at <https://doi.org/10.1007/s00170-021-07753-5>.

Numerical analysis of the Ti6Al4V behavior based on the definition of a new phenomenological model

Mariem Yaich^{a,b,*}, Yessine Ayed^a, Guenael Germain^a, and Zoubeir Bouaziz^b

^a *Arts et Métiers ParisTech, LAMPA, 2 bd du Ronceray, 49035 Angers CEDEX, France*

^b *Université de Sfax, Ecole Nationale d'Ingénieurs de Sfax, Laboratoire de Mécanique des Fluides Appliquées, Génie des Procédés et Environnement, LR11ES57, 3 038 Sfax, Tunisia*

Abstract

The finite element modeling is significantly depended on the accurate prediction of the thermomechanical material behavior. In order to increase the accuracy of numerical simulations, a new phenomenological model is proposed in this study. Its mathematical formulation allows accurate predictions of the Ti6Al4V sensitivity to the strain rate and the temperature, while maintaining a low identification cost of its constitutive coefficients. Its implementation in the Abaqus® software is carried out based on the developed VUMAT. The subroutine robustness is investigated in the case of the modeling of uniaxial tensile and impact tests. A 3D numerical analysis of the Ti6Al4V machining is set up based on the definition of the rheological Johnson-Cook model and the proposed one. Experimental orthogonal machining tests are also established for several cutting conditions. An important sensitivity of the chip serration, segments geometry and the cutting forces to the feed rate is pointed out. Comparisons of the numerical results obtained with both models are carried out. Interesting agreements with the experimental results are guaranteed with the new phenomenological model, which is not the case of the Johnson-Cook empirical law. In addition, intuitive insights about the effect of the cutting conditions on the material flow towards the workpiece edges and the side burr geometry are provided with the 3D numerical modeling. The results presented in this study point out the inability of the 2D numerical simulations to accurately predict the phenomena induced during the machining process, even in the case of an orthogonal machining.

* *Corresponding author: M.Yaich*
E-mail address: yaichmariem@gmail.com

Keywords

Ti6Al4V; VUMAT; Constitutive model; Chip segmentation; Orthogonal machining

1 Introduction

The commonly used biphasic Ti6Al4V titanium alloy is known for its interesting strength-to-weight ratio, as well as its excellent resistance to corrosion and its significant creep properties. However, its low thermal conductivity and its significant mechanical properties, even for high temperatures are responsible of its poor machinability [1]. The important vibrations and the concentration of pronounced heats in very thin cutting zones, which are encountered during the machining process of this titanium alloy, result in an accelerated tool wear, mainly in the case of high chemical affinity with the cutting tool material [2]. In order to understand the physical phenomena induced during the machining process, several experimental investigations have been performed in the literature review [3] [4]. Different experimental devices (e.g. optical microscopy, high frame rate camera, etc.) have been used to enable the instantaneous access to instantaneous and local physical information, during the chip formation. In the experimental study of Pottier et al. [4], a new method based on the submillimeter procedure post-processing has been proposed to determine the strain field in the segmented chip. However, the investigation of crack propagation within segmented chips has been not possible, when only experimental tests have been carried out. The serious efforts, which have been performed in the aim to increase the reliability of experimental in-situ and post-mortem equipment, are still insufficient for precious and instantaneous local measurements. Therefore, numerical simulations of the machining processes are required, in addition to experimental tests, to provide important information about the phenomena induced in the cutting zones during the chip formation [5].

The availability of powerful and efficient commercial codes have encouraged the establishment of numerical simulations, mainly in the case of the machining process where important dynamic and non-linear conditions are taking place. Their ability to

reduce both time and cost of the analysis, while providing significant information, have encouraged their widespread adoption in the literature review. The finite element (FE) modeling of the machining has been focused on the prediction of the chip segmentation, the cutting forces, the material tribology, the surface integrity, the tool edge preparation effects, etc. [6–12]. However, the adequate definition of the numerical model parameters and the workpiece material behavior is crucial for a reliable FE modeling. Several constitutive models have been proposed in the literature review [13–15]. These models are mainly classified in three categories: the empirical, the semi-empirical and the physically-based models incorporating the physical phenomena and the microstructure changes undergone within the machined material. The most evolved constitutive criteria are the physically-based material models since they are based on the physics of the material deformation [16]. Internal variables are defined in the aim to take into account the effects of the deformation history and/or the material microstructure changes (e.g. the dislocation density, its orientations, the grain size, etc.). Despite the ability of these constitutive laws to reliably reproduce the material behavior, they have been uncommonly used to model severe dynamic processes (e.g. the machining process). The challenge has been to accurately identify the constitutive parameters for several loading conditions. Special and expensive experimental equipment have been required. In addition, the numerical implementation of the physically-based models, with heavily coupled terms, in the commercial codes has presented a genuine task. On the other hand, the semi-empirical models, which are characterized by a less complex mathematical formulation while taking into account the effects of some metallurgical aspects, have been an interesting alternative. Although the internal variables have not been used, this constitutive models' category has allowed a well prediction of the material behavior. However, some problems related to the implementation of these models in the numerical

analysis and the identification of their several coupled constitutive coefficients have been raised. On the other hand, the common use of empirical models for the modeling of dynamic forming processes (e.g. the machining process) has been underlined in the literature review [16]. The thermo-visco-plastic Johnson-Cook (JC) model [17] have been used in many numerical investigations focused on the modeling of the machining process [7, 18–21]. Its mathematical expression is given by Eq. (1). The material flow stress is expressed through three uncoupled terms: the Ludwik plastic hardening term $H(\varepsilon_p)$ [22], the strain rate logarithmic sensitivity term $G(\dot{\varepsilon})$ and the thermal softening term $F(T)$ [17] (see Eqs. (2), (3) and (4) respectively). The outstanding success of the JC empirical model is due to its implementation in many commercial codes, as well as its adequacy to high strain rates. In addition, its uncoupled terms and the low number of its parameters have facilitated its identification. However, the main challenge is summarized in accurately identifying the model parameters, which depend on the used experimental tests and the applied loading conditions [7, 9]. A proper fitting of the experimental flow stress-plastic strain curves for high plastic strains, low strain rates and different temperature ranges is required for a reliable numerical analysis, mainly in the case of the machining modeling. The inability of the JC rheological model to suitably predict the thermo-mechanical behavior of the Ti17 titanium alloy for high temperatures and important strain rates, up to 1000°C and 10^5 s^{-1} respectively, has been highlighted in the literature [23]. Moreover, the definition of the JC strain rate sensitivity term (see Eq. (3)) for quasi-static loading conditions gives rise to numerical problems [24]. In order to avoid the FE modeling divergence, a discontinuous regularization is used by the commercial code Abaqus® (see Eq. (3)). Moreover, Liu et al. [25] have underlined the inability of the JC thermal softening law to suitably predict the dual phase steel plate DP600 behavior for temperatures ranged between 300K and 1200K.

$$\sigma_{JC} = H(\varepsilon_p) \times G(\dot{\varepsilon}) \times F(T) \quad (1)$$

$$H(\varepsilon) = A + B \times \varepsilon_p^n \quad (2)$$

$$G(\dot{\varepsilon}) = \begin{cases} 1 & (\text{For: } \dot{\varepsilon} \leq \dot{\varepsilon}_0) \\ 1 + C \times \ln\left(\frac{\dot{\varepsilon}}{\dot{\varepsilon}_0}\right) & (\text{For: } \dot{\varepsilon} > \dot{\varepsilon}_0) \end{cases} \quad (3)$$

$$F(T) = \begin{cases} 1 & (\text{For: } T < T_{room}) \\ 1 - \left(\frac{T - T_{room}}{T_{melt} - T_{room}}\right)^m & (\text{For: } T_{room} \leq T \leq T_{melt}) \\ 0 & (\text{For: } T > T_{melt}) \end{cases} \quad (4)$$

where, ε_p , $\dot{\varepsilon}$ and T are the equivalent plastic strain, the equivalent strain rate and the temperature, respectively. $\dot{\varepsilon}_0$ is the reference equivalent plastic strain rate corresponding to the transition from static loadings to dynamic ones. T_{room} and T_{melt} are the room temperature and the melting one, which are equal to 293K and 1943K respectively. A , B , n , C and m are the initial material yield stress at room temperature, the Ludwik hardening modulus, the Ludwik hardening exponent, the JC strain rate sensitivity coefficient and the JC thermal softening coefficient, respectively.

Despite the several efforts to improve the FE modeling reliability, the definition of an accurate constitutive model, which allows the proper prediction of the material behavior while ensuring a controlled coefficients identification and an easier implementation in the numerical software, is heavily required. In this study, a new phenomenological model based on the previous investigation of Ayed et al. [23] is proposed. An exponential viscosity term and a modified JC thermal softening law are used to respectively reproduce the Ti6Al4V titanium alloy behavior under several strain rates and temperatures. The identification of constitutive coefficients is performed based on the experimental compression tests of Braham-Bouchnak [26]. The non-linear

regression method is used. Comparisons between the experimental flow stress-plastic strain curves and the computed ones are carried out to investigate the advantageous of proposed modifications. The validation of the new phenomenological model is performed, for several loading conditions. Its implementation in the Abaqus®/Explicit software is done, where a user-material subroutine VUMAT is developed. Numerical simulations of uniaxial tensile tests and very dynamic impact tests are set up. The experimental orthogonal Ti6Al4V machining process is carried out, for different cutting conditions. 3D numerical simulations are set up and the efficiency of the proposed rheological model in terms of accurately predicting the chip segmentation and the cutting forces is studied. Attention is also paid to the investigation of the material flow towards the workpiece sides. The sensitivity of the side burrs to the cutting conditions is underlined.

2 Definition and identification of investigated rheological models

A new material model based on the commonly used JC empirical and uncoupled law (Eq. (1)) was proposed. As shown by Eq. (5), the material sensitivity to the plastic strain was predicted based on the Ludwik law. Whereas, new strain rate and temperature sensitivity terms were defined. An exponential function was used instead of the logarithmic JC strain rate sensitivity term. In addition, the constant coefficient m of the ‘standard’ JC model was replaced by a new function $m(T)$ that evolved with the temperature rise (see Eq. (6)) in order to take into account the thermal softening effects on the Ti6Al4V behavior, for wide temperature ranges.

$$\sigma = \left(A + B \times \bar{\varepsilon}^n \right) \times \left(Y_0 + A_0 \times \exp \left(R_0 \frac{\dot{\varepsilon}}{\dot{\varepsilon}_0} \right) \right) \times \left(1 - \left(\frac{T - T_{room}}{T_{melt} - T_{room}} \right)^{m(T)} \right) \quad (\text{For: } T_{room} \leq T \leq T_{melt}) \quad (5)$$

where A , B and n are the plastic strain sensitivity coefficients and they correspond to the initial yield stress at the reference strain rate and the initial temperature, the Ludwik hardening modulus and its exponent, respectively. Y_0 , A_0 and R_0 are the strain rate sensitivity coefficients. $m(T)$ is the thermal softening sensitivity exponent function and it is written as follow.

$$m(T) = m_1 \times \left(1 - \exp\left(m_2 (T - T_\beta)\right) \right) \quad (6)$$

where T_β is the β -transus temperature and it is equal to 1253K for the Ti6Al4V titanium alloy [26]. m_1 and m_2 are the thermal softening coefficients of the proposed material constitutive law.

In this study, the experimental compression tests of the literature [27] were used for the constitutive models identification. In these tests, several reference speeds, which are ranged between 0.1 mm.s⁻¹ and 1000 mm.s⁻¹, and different initial temperatures (293K, 473K, 673K, 873K and 1073K), have been defined. The identification of the JC empirical model (see Eq. (1)), the modified one proposed by Ayed et al. [23] (MJC1) (see Eq.(7)) and the new rheological model given by Eq. (5) (MJC2) was done based on the same experimental tests.

$$\sigma = \left(A + B \times \bar{\varepsilon}^n \right) \times \left(1 + C(\bar{\dot{\varepsilon}}) \times \ln\left(\frac{\bar{\dot{\varepsilon}}}{\dot{\varepsilon}_0}\right) \right) \times \left(1 - \left(\frac{T - T_{room}}{T_{melt} - T_{room}} \right)^{m(T)} \right) \quad (\text{For: } T_{room} \leq T \leq T_{melt}) \quad (7)$$

where $C(\bar{\dot{\varepsilon}})$ and $m(T)$ are the viscosity and the thermal softening functions, which expressions are given by Eqs. (8) and (6) respectively.

$$C(\bar{\dot{\varepsilon}}) = C_1 \times \exp\left(C_2 \times \ln\left(\frac{\bar{\dot{\varepsilon}}}{\dot{\varepsilon}_0}\right) \right) \quad (8)$$

The non-linear regression method was used in the identification of all studied rheological models. The optimal set of constitutive coefficients ($P_{JC} = \{A, B, n, C, m\}$),

$P_{MJC1} = \{A, B, n, C_1, C_2, m\}$ and $P_{MJC2} = \{A, B, n, Y_0, A_0, R_0, m_1, m_2\}$) were determined by minimizing in a least square sense the errors between the experimental flow stress-plastic strain curves and the computed ones for the same loading conditions. The general error function given by Eq.(9) was defined in this study. A specific iterative identification procedure was used for a better adjustment of the material coefficients, thus more reliable fitting of experimental curves. It consisted of three steps. First of all, the isotropic hardening coefficients (A , B and n) were determined. Because of the self-heating of the specimen material induced during dynamic tests, the material thermal softening parameters were secondly identified based on the stress-plastic strain curves corresponding to the reference strain rate and several initial temperatures. The strain rate sensitivity coefficients were finally determined. Table 1 regroups the constitutive coefficients of all compared rheological models.

Table 1 Constitutive model coefficients based on the experimental compression tests

Models	Constitutive coefficients							
JC	A (MPa)	B (MPa)	n	C				m
	518.54	941.12	0.16	0.0087				0.58
MJC1	A (MPa)	B (MPa)	n	C_1	C_2	m_1		m_2
	518.54	941.12	0.16	0.0027	0.198	1.628		0.001
MJC2	A (MPa)	B (MPa)	n	Y_0	A_0	R_0	m_1	m_2
	518.54	941.12	0.16	1.155	-0.124	-0.007	1.628	0.001

$$Q = \sum_{i=1}^{n_i} \gamma_i \times [(\sigma_c)_i - (\sigma_{\text{exp}})_i]^2 \quad (9)$$

where n_i is the total number of experimental measurements for all investigated loading conditions. γ_i is the weighting factor, which mathematical expression is given by Eq. (10). σ_c is the computed flow stress and σ_{exp} is the experimental one.

$$\gamma_i = 1 / \sum_{i=1}^{n_i} [(\sigma_{\text{exp}})_i]^2 \quad (10)$$

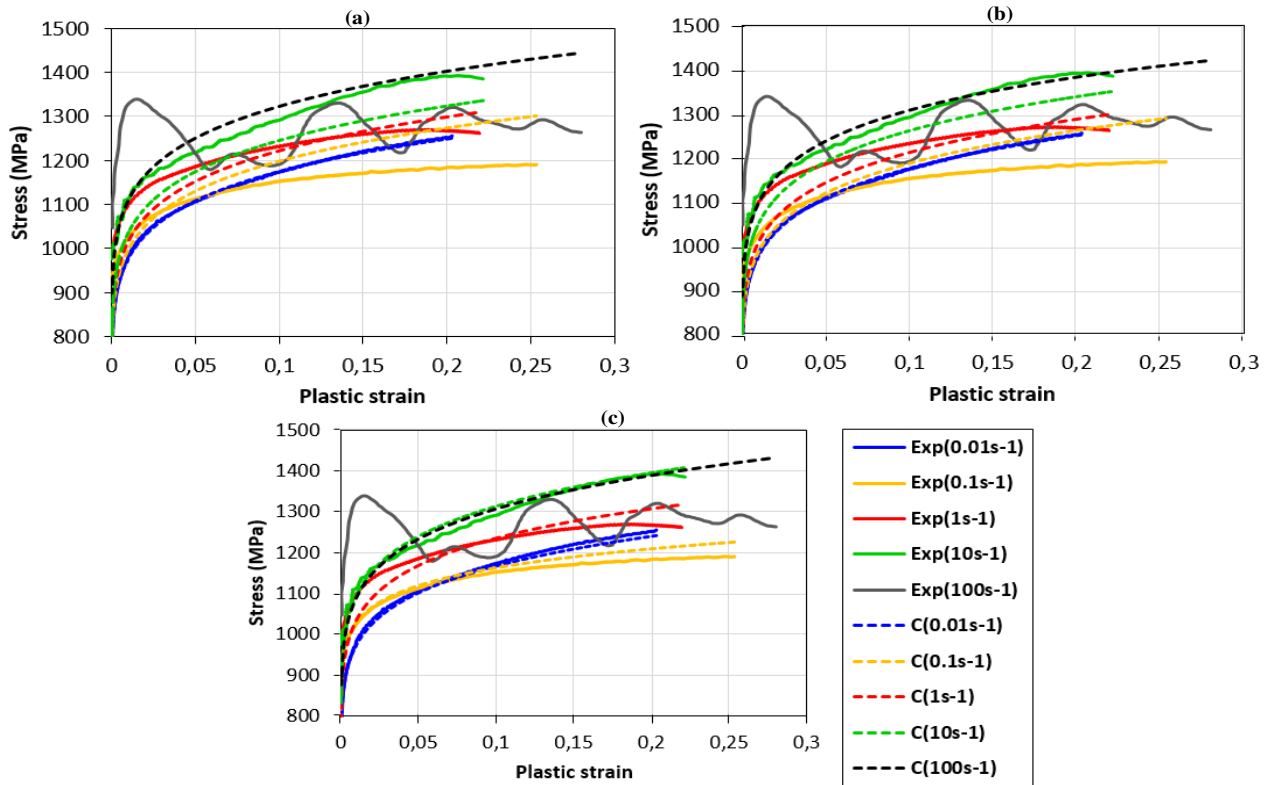


Fig. 1 Comparison of the experimental true stress-plastic strain curves obtained for different strain rates and the room temperature to those computed with different rheological models: (a) JC, (b) MJC1 and (c) MJC2 models

The ability of the compared rheological models in accurately reproducing the experimental material behavior was compared. Fig. 1 illustrates the experimental flow stress-plastic strain curves and those computed based on the definition of the identified constitutive coefficients, for different initial strain rates. The definition of the empirical JC model resulted in the most mismatched results. An average relative error about 17% was computed while its value did not exceed 6.12% and 5.7% in the case of the modified model of Ayed et al. [23] and the new one proposed in this study. For all investigated rheological models, the computed flow stresses were in disagreement with the experimental one in the case of $\bar{\dot{\epsilon}} = 100s^{-1}$ (see Fig. 1). For lower strain rates, the MJC2 model enabled few improvements of the JC empirical model predictions. However, flow

stress very close to the experimental ones were computed with the MJC2 model, for strain rates ranged between $0.01s^{-1}$ and $10s^{-1}$. The new viscosity law allowed more accurate prediction of the Ti6Al4V alloy behavior without increasing the identification cost, where the same experimental compression tests were used for the identification of its constitutive coefficients. In addition, it enabled the overcoming of the numerical divergence problems due to the definition of the logarithmic function used by the JC strain rate sensitivity law for $\bar{\dot{\epsilon}} < \dot{\epsilon}_0$.

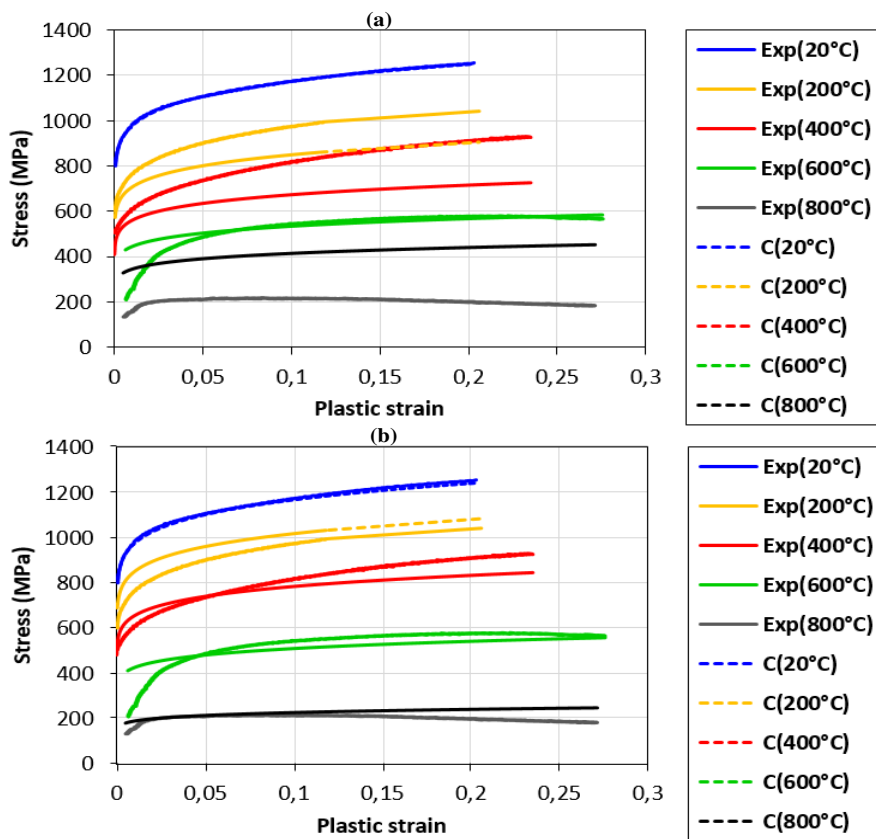


Fig. 2 Experimental and computed stress-plastic strain curves corresponding to different initial temperatures and a reference strain rate of $0.01s^{-1}$: (a) JC and (b) MJC2 models

Important errors between the experimental stress-plastic strain curves of the literature and the computed ones based on the empirical JC model definition are illustrated in Fig. 2. These mismatched results were due to the definition of a constant thermal softening coefficient m , which was unable to accurately reproduce the

temperature effects on the Ti6Al4V titanium alloy. For temperatures ranged 473K and 1073K, a pronounced variation of the JC thermal softening coefficient was underlined. m values were ranged between 0.25 and 0.9 as illustrated by the blue curve of Fig. 3. This variation was neglected due to the definition of the same JC thermal softening coefficient for all temperatures. Contrariwise, the modifications made to the JC thermal softening law enabled more reliable predictions of the Ti6Al4V behavior for different temperatures (see Fig. 2). The definition of the $m(T)$ function allowed to properly take into account the variation of the m coefficient with temperature (see Fig. 3).

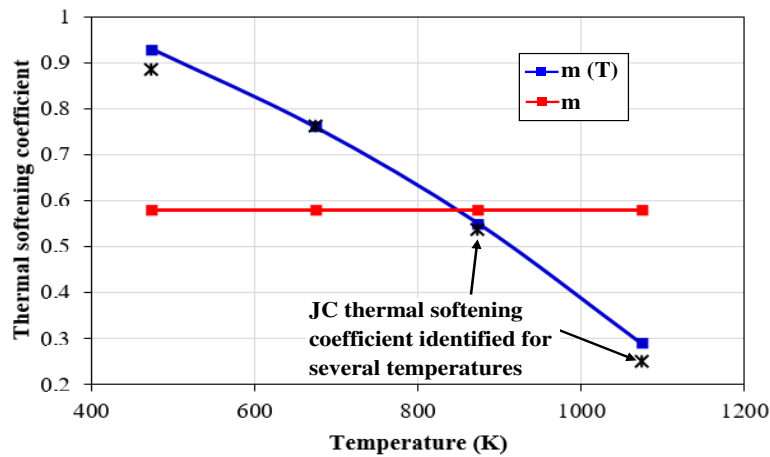


Fig. 3 Comparison of the JC thermal softening coefficient to the proposed $m(T)$ function

These preliminary results pointed out the efficiency of proposed rheological model in terms of allowing more reliable predictions of Ti6Al4V behavior for several loading conditions without increasing the constitutive coefficient identification cost.

3 VUMAT definition and validation

3.1 VUMAT definition

The implementation of the empirical JC model and the proposed one in the FE software Abaqus® was done. The explicit scheme suitable for dynamic and important nonlinear conditions, similar to those induced during the Ti6Al4V titanium alloy machining, was adopted. A user material subroutine VUMAT was developed. According to Chattonjai

[28], the definition of the global stiffness matrix in this subroutine and its update are not required, giving rise to a more straightforward implementation of the constitutive material models. The material parameters were defined in a vector form and the components' order was imperatively respected. The stress tensor components and the state variables were locally updated for all mesh elements. The fact that severe dynamic phenomena are involved during the Ti6Al4V machining, hindering consequently the modeling convergence, sufficiently small increments were used. In this study, an assumption of isotropic material behavior was made the fact that no cyclic loadings, and thereby Bauschinger effects, were investigated. The von Mises plasticity criterion, which is widely used in the modeling of the material plastic hardening deformation, was defined. A scalar yield function f was computed (see Eq. (11)) and the elastoplastic transition was verified at every time increment Δt . If $f < 0$, an elastic (reversible) material deformation was assumed and the von Mises equivalent stress increased from zero to the initial yield surface (see Fig. 4). However, a plastic deformation was taking place once $f \geq 0$ and an increase of the yield surface was taking place. Hence, a massive proliferation of dislocations (stacking defects) within the metal crystal were encountered [29, 30]. These significant irreversible movements of dislocations were underlined during the machining of the Ti6Al4V alloy according to Yang and Liu [31]. Hence, severe changes of the material properties were noted and a drift of the $\sigma_{(t+\Delta t)}$ stress was obtained (see Fig. 4). Indeed, a correction of the positive yield function based on the classical return mapping algorithm was done.

$$f = \bar{\sigma}_{pr} - \sigma_y(\bar{\varepsilon}, \bar{\dot{\varepsilon}}, T) \quad (11)$$

where, $\sigma_y(\bar{\varepsilon}, \dot{\bar{\varepsilon}}, T)$ and $\bar{\sigma}_{pr}$ are the yield stress and the equivalent predictor stress, respectively. In current study, the $\sigma_y(\bar{\varepsilon}, \dot{\bar{\varepsilon}}, T)$ stress was computed based on the JC rheological model or the proposed one given by Eq. (5).

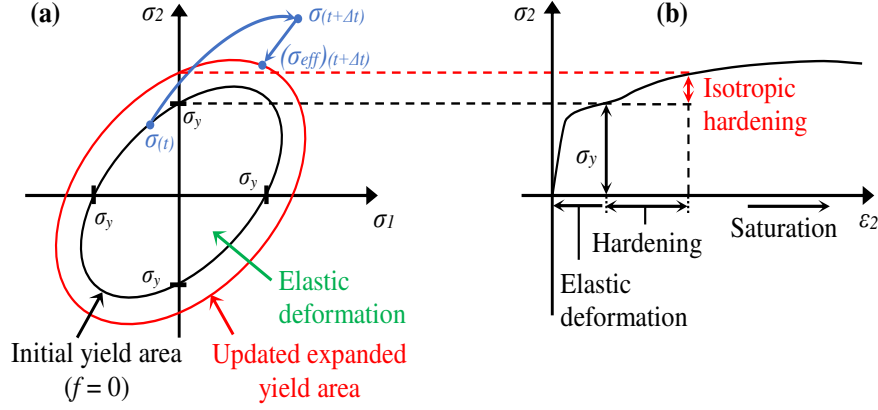


Fig. 4 Schematic representation of (a) yield areas in the plane stress and (b) the uniaxial stress-strain curves (case of an isotropic hardening plasticity)

The general approach adopted to explicitly implement the compared material models is illustrated in Fig. 5. The state of every finite element at the beginning of each time frame was assumed as the reference state. The strain increments $\Delta\varepsilon_{ij}$, the components of the stress tensor σ_{ij} and the state variables were recovered for all elements mesh and they were used in the material behavior prediction. A plastic correction factor m_{corr} given by Eq. (12) was defined in order to allow the radial return mapping of the integration scheme, and thereby to bring back the updated stress onto the yield area. Based on the numerical analysis of Pipard [32], the plastic correction factor was only applied to the deviatoric stress and the effective stress tensor $(\sigma_{eff})_{(t+\Delta t)}$ was explicitly computed (see Eq. (13)). This assumption was justified by the incompressibility conditions of nonporous metals, which plastically deform without any volume change.

$$m_{corr} = \frac{\left(\sigma_y(\bar{\varepsilon}, \dot{\bar{\varepsilon}}, T)\right)_{(t+\Delta t)}}{\left(\bar{\sigma}_{pr}\right)_{(t+\Delta t)}} \quad (12)$$

where $(\sigma_y(\bar{\varepsilon}, \dot{\varepsilon}, T))_{(t+\Delta t)}$ and $(\bar{\sigma}_{pr})_{(t+\Delta t)}$ are the updated yield stress and the equivalent elastic predictor stress, respectively.

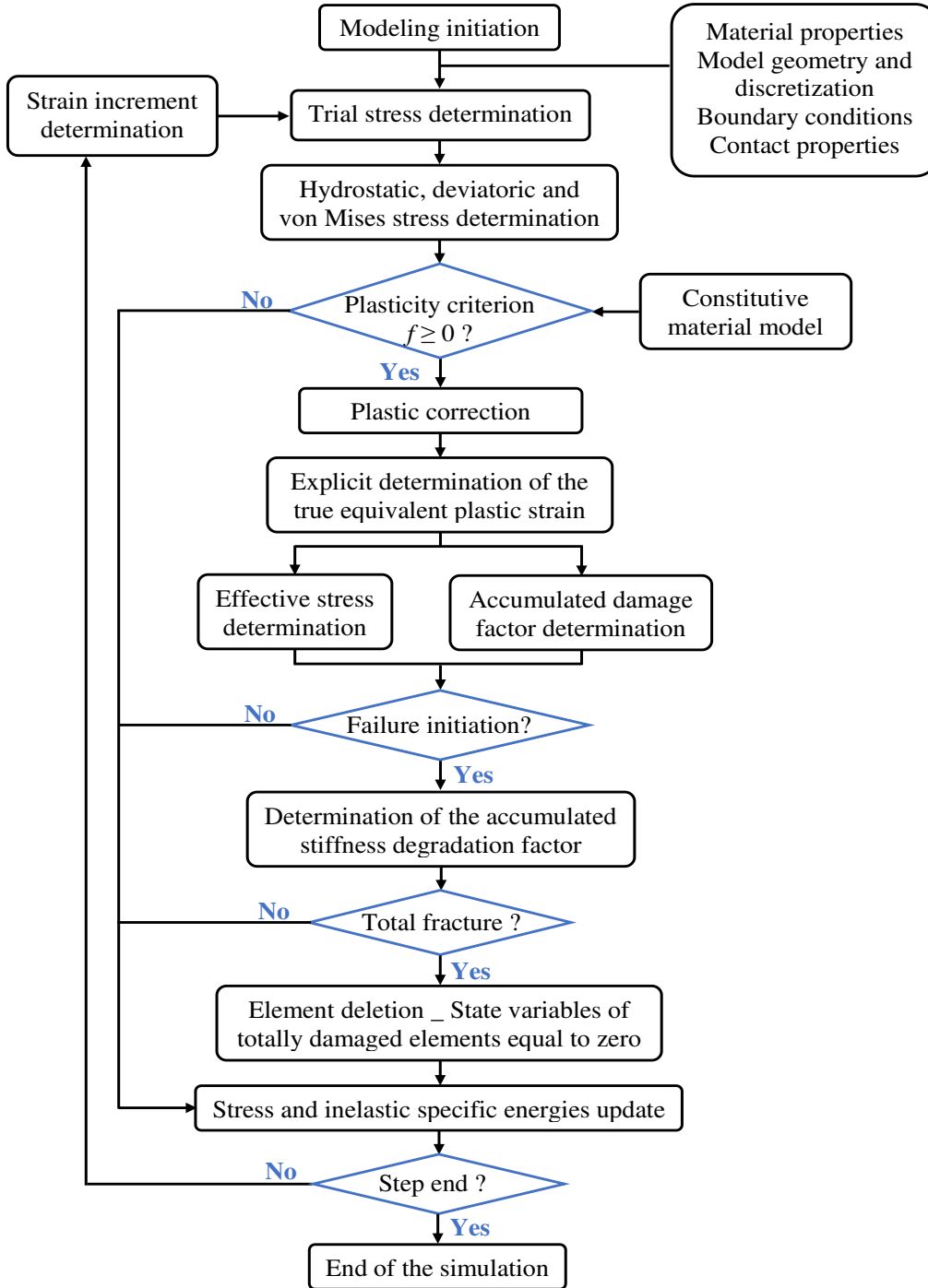


Fig. 5 Flowchart of the VUMAT set up to implement the constitutive models in FE software Abaqus®/Explicit

$$[\sigma_{eff}]_{(t+\Delta t)} = (\sigma^h)_{(t+\Delta t)} \times [I] + m_{corr} \times [\sigma_{pr}^{dev}]_{(t+\Delta t)} \quad (13)$$

where $(\sigma^h)_{(t+\Delta t)}$ and m_{corr} are the updated hydrostatic stress and the correction factor, respectively. $[\sigma_{pr}^{dev}]_{(t+\Delta t)}$ is the updated deviatoric stress tensor.

The equivalent plastic strain increment $(\Delta\bar{\varepsilon}_p)_{(t+\Delta t)}$ was explicitly determined based on Eq. (14). The deviatoric plastic strain tensor $[\Delta\varepsilon_p^{dev}]_{(t+\Delta t)}$ expression given by Eq. (15) was determined and used for the $(\Delta\bar{\varepsilon}_p)_{(t+\Delta t)}$ computation (see Eq. (16)). Finally, the increment of the plastic strain $(\varepsilon_p)_{(t+\Delta t)}$ and the yield stress $(\sigma_y(\bar{\varepsilon}, \dot{\bar{\varepsilon}}, T))_{(t+\Delta t)}$ were updated. As shown by Eq. (17), a linear hardening was assumed. This assumption was justified by the explicit integration scheme initially considered and the extremely defined small increment time. Therefore, the highest order terms were neglected and the plastic strain increment was computed using Eq. (18).

$$(\Delta\varepsilon_p)_{(t+\Delta t)} = \sqrt{\frac{2}{3} [\Delta\varepsilon_p^{dev}]_{(t+\Delta t)} : [\Delta\varepsilon_p^{dev}]_{(t+\Delta t)}} \quad (14)$$

where $[\Delta\varepsilon_p^{dev}]_{(t+\Delta t)}$ is the deviatoric plastic strain tensor.

$$[\Delta\varepsilon_p^{dev}]_{(t+\Delta t)} = \left(\frac{1 - m_{corr}}{2 \times \mu_{Lame}} \right) \times [\sigma_{pr}^{dev}]_{(t+\Delta t)} \quad (15)$$

where μ_{Lame} is the Lamé factor.

$$(\Delta\bar{\varepsilon}_p)_{(t+\Delta t)} = \left(\frac{1 - m_{corr}}{3 \times \mu_{Lame}} \right) \times (\bar{\sigma}_{pr})_{(t+\Delta t)} = \frac{(\bar{\sigma}_{pr})_{(t+\Delta t)} - (\sigma_y(\bar{\varepsilon}, \dot{\bar{\varepsilon}}, T))_{(t+\Delta t)}}{3 \times \mu_{Lame}} \quad (16)$$

$$(\sigma_y(\bar{\varepsilon}, \dot{\bar{\varepsilon}}, T))_{(t+\Delta t)} = (\sigma_y(\bar{\varepsilon}, \dot{\bar{\varepsilon}}, T))_{(t)} + \left(\frac{d\sigma_y(\bar{\varepsilon}, \dot{\bar{\varepsilon}}, T)}{d\varepsilon} \right)_{(t)} \times (\Delta\bar{\varepsilon}_p)_{(t+\Delta t)} + \dots \quad (17)$$

$$\left(\Delta\bar{\varepsilon}_p\right)_{(t+\Delta t)} = \frac{\left(\bar{\sigma}_{pr}\right)_{(t+\Delta t)} - \left(\sigma_y\left(\bar{\varepsilon}, \bar{\dot{\varepsilon}}, T\right)\right)_{(t)}}{3 \times \mu_{Lame} + \left(\frac{d\sigma_y\left(\bar{\varepsilon}, \bar{\dot{\varepsilon}}, T\right)}{d\varepsilon}\right)_{(t)}} \quad (18)$$

where $\left(\frac{d\sigma_y\left(\bar{\varepsilon}, \bar{\dot{\varepsilon}}, T\right)}{d\varepsilon}\right)$ is the yield hardening parameter.

In this study, the JC damage model [33] was defined to predict the damage initiation in the finite elements once $w=1$ (see Eqs. (19) and (20)). Therefore, a progressive decrease of the flow stress was taking place until reaching the total degradation of the mesh. Eq (21) was used to take into account the failure effects on the damaged material behavior. The modeling of the progressive degradation of the material stiffness was done based on both linear and exponential forms (given by Eqs. (22) and (23) respectively). Finally, the state variables, the specific internal energy and the dissipated inelastic one were updated.

$$\omega_{(t+\Delta t)} = \omega_{(t)} + \Delta\omega_{(t+\Delta t)} = \omega_{(t)} + \frac{\Delta\varepsilon_{(t+\Delta t)}}{\left(\varepsilon_{JCD}\right)_{(t+\Delta t)}} \quad (19)$$

where $\left(\varepsilon_{JCD}\right)_{(t+\Delta t)}$ is the plastic strain corresponding to the damage initiation in the finite element and it was computed as follow:

$$\left(\varepsilon_{JCD}\right)_{(t+\Delta t)} = \left[D_1 + D_2 \times \exp\left(D_3 \frac{\left(\sigma_h\right)_{(t+\Delta t)}}{\left(\sigma_{pr}\right)_{(t+\Delta t)}} \right) \right] \times \left[1 + D_4 \times \ln\left(\frac{\dot{\varepsilon}_{(t+\Delta t)}}{\dot{\varepsilon}_0} \right) \right] \times \left[1 + D_5 \times \left(\frac{T_{(t+\Delta t)} - T_0}{T_m - T_0} \right) \right] \quad (20)$$

where D_i ($i = 1, 2, 3, 4, \text{ and } 5$) are the JC damage coefficients which values are regrouped in Table 2.

$$\left[\sigma_{eff} \right]_{(t+\Delta t)} = \left(1 - \left(D_{ev} \right)_{(t+\Delta t)} \right) \times \left[\tilde{\sigma} \right]_{(t+\Delta t)} \quad (21)$$

where, $\left[\tilde{\sigma} \right]_{(t+\Delta t)}$ is the stress tensor if the damage effect was neglected. $\left(D_{ev} \right)_{(t+\Delta t)}$ is the damage evolution parameter at $t+\Delta t$ (see Eqs. (22) and (23)).

$$(D_{ev})_{(t+\Delta t)} = \frac{(\Delta \bar{u}_p)_{(t+\Delta t)}}{\bar{u}_f} = \frac{L \times (\varepsilon_p)_{(t+\Delta t)}}{\bar{u}_f} \quad (22)$$

$$(D_{ev})_{(t+\Delta t)} = 1 - \exp\left(-\int_0^{\bar{u}_p} \left(\frac{\sigma_{y_0}(\bar{\varepsilon}, \bar{\varepsilon}, T)}{G_f}\right) \times d\bar{u}_p\right) \quad (23)$$

where \bar{u}_p is the equivalent plastic displacement. \bar{u}_f is the equivalent material displacement at failure (see Eq. (24)).

$$u_f = \frac{2 \times G_f}{\sigma_{y_0}(\bar{\varepsilon}, \bar{\varepsilon}, T)} \quad (24)$$

where G_f is the failure energy and $\sigma_{y_0}(\bar{\varepsilon}, \bar{\varepsilon}, T)$ is the yield stress at the damage initiation.

Table 2 JC damage coefficients of the Ti6Al4V titanium alloy [34]

JC damage coefficient	D_1	D_2	D_3	D_4	D_5
Value	-0.09	0.25	-0.5	0.014	3.87

3.2 VUMAT validation

The reliability of the user-material subroutine was verified for several loading conditions. Numerical simulations of uniaxial tensile tests along the X-direction were firstly set up in the FE software Abaqus®. The model geometry and the boundary conditions are illustrated in Fig. 6-a. Tensile velocities and initial temperatures ranged between 0.01 mm/s – 100 mm/s and 293K – 1073K, respectively, were defined. The model discretization was carried out based on the definition of one 3D 8-node thermally coupled finite element (C3D8RT) was used. Displacement-temperature coupling conditions and a reduced integration scheme were assumed.

The accuracy of the performed implementations in the case of ultra-high dynamic conditions was also investigated. Numerical simulations of the axisymmetric Taylor impact test under strain rates of 200 m.s^{-1} and 300 m.s^{-1} were performed. This test consisted in the modeling of the projectile compression against a hardened rigid target. During the impact test, the end-face of the cylindrical specimen was subjected to very important plastic strains. In this study, an initial temperature of 293K was defined. Axial displacements of the projectile were permitted, while radial displacements were constrained (see Fig. 6-b). The model discretisation was done based on the definition of 270 quadrilateral axisymmetric CAX4RT mesh. A reduced integration and coupled temperature-displacement conditions were assumed.

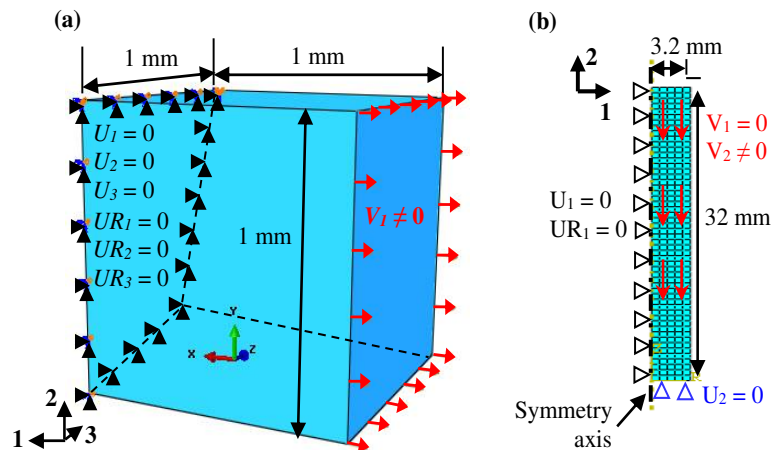


Fig. 6 Model geometry and boundary conditions of (a) the 3D tensile test and (b) the 2D axisymmetric impact test

In current study, no comparisons with the experimental results were set up the fact that the main purpose was to verify the suitability of performed implementations in terms of reliably reproducing the numerical results directly modeled with the FE code Abaqus®, for the same loading conditions. Therefore, the JC empirical model [17], the JC damage initiation law [33] and the failure evolution criteria (given by Eq. (22) and (23)), which are available in the Abaqus® library, were implemented in the VUMAT and

used in this comparative analysis. The constitutive coefficients regrouped in the Tables 1 and 2 were defined. The physical material properties of the Ti6Al4V alloy defined in the numerical simulations corresponded to those used in the FE analysis of Yaich et al. [21]. An assumption of adiabatic conditions was made and a Taylor-Quinney parameter of 0.9 was defined.

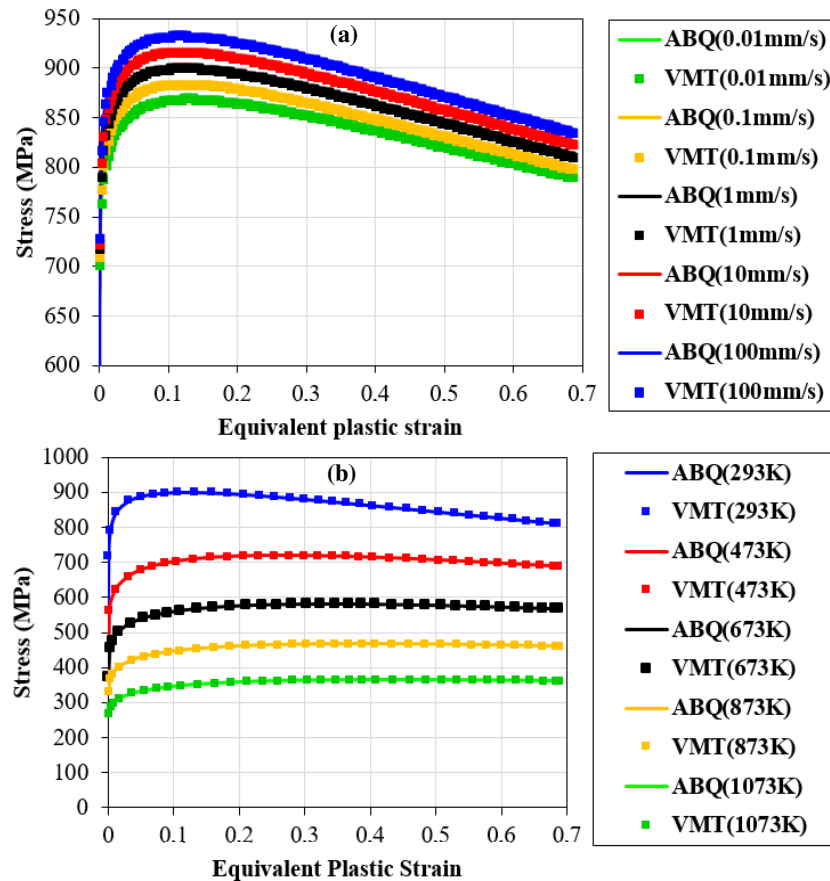


Fig. 7 Numerical stress-plastic strain curves predicted when the empirical JC model of the Abaqus® library (ABQ) or that implemented in the VUMAT (VMT) was defined: (a) $T_0 = 293$ K and (b) $V = 1$ mm/s

Comparisons of the numerical curves of von Mises stresses and damage evolution variables, which were directly modeled with the FE software Abaqus®, to those obtained when the VUMAT was defined, are illustrated in Fig. 7 and Fig. 8 respectively. Important agreements between the numerical results of uniaxial tensile tests were noted in the case of the JC empirical model definition. In addition, the definition of the VUMAT allowed

important agreements with the numerical results modeled directly with Abaqus®, for both linear and exponential failure evolution (see Fig. 8).

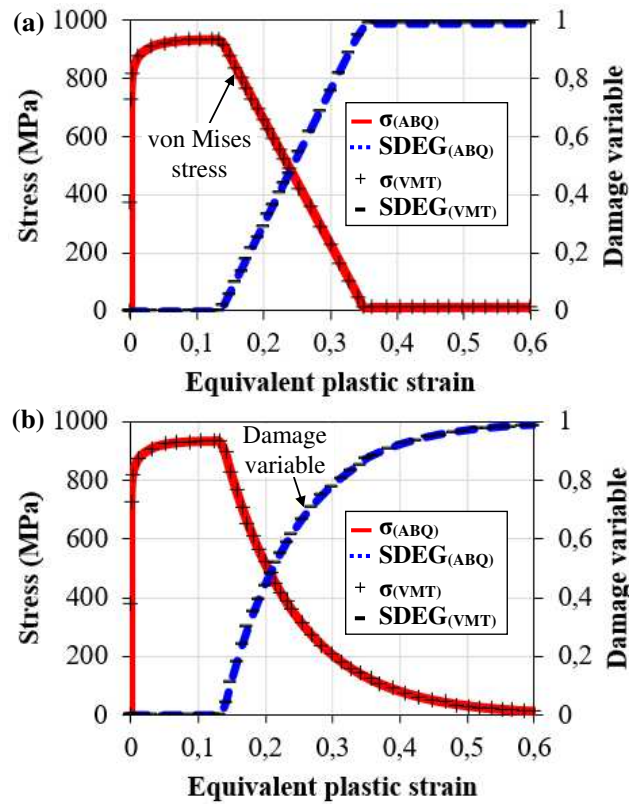


Fig. 8 Instantaneous Von Mises stress and damage variable (SDEG) ($v = 100\text{mm} / s$): (a) linear and (b) exponential failure evolution models

Fig. 9 illustrates the equivalent plastic strain (PEEQ or SDV1) and the damage variable (SDEG or SDV5) predicted in the deformed projectile. Both methods used for the impact test modeling resulted in a pronounced plastic strain concentration at the projectile bottom face followed by the material damage initiation and its evolution, mainly around the symmetry axis. In addition, the deformed projectile geometries, which were predicted with the constitutive models available in Abaqus® and the same ones implemented in VUMAT, were almost superposed (see Fig. 10). An extremely deformed projectile part was obtained resulting in the modeling of a mushroom shape in the bottom surface of the specimen. An intermediate part of the projectile was also noted between the almost undeformed part and the extremely deformed one. Interesting correlation

levels in terms of the computed final height and radius were highlighted. For both FE modeling methods, a final height and radius of the deformed cylinder of 1.3mm and 300 μm , respectively, was computed in the case of an impact velocity of 300 $\text{m}\cdot\text{s}^{-1}$. These important agreements between the numerical results of the built-in Abaqus® material models and the programmed ones emphasized the accuracy of the carried out implementations, for both quasi-static to ultra-high dynamic conditions.

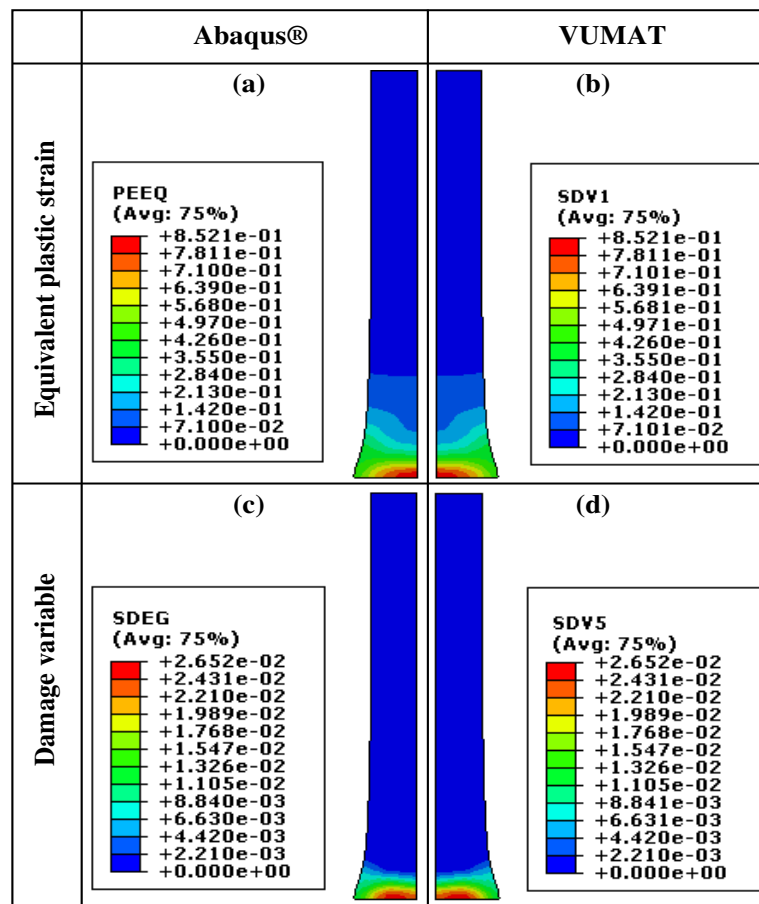


Fig. 9 Numerical deformed projectile predicted with (a, c) Abaqus® and (b, d) through the VUMAT definition ($V = 200 \text{ m}\cdot\text{s}^{-1}$ and $T_0 = 293\text{K}$): (a-b) Equivalent plastic strain (c-d) and damage evolution variable

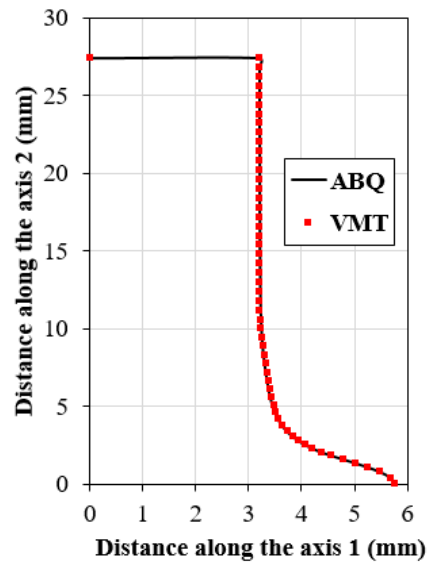


Fig. 10 Deformed projectile geometry directly modeled with Abaqus® (ABQ) or through the VUMAT definition (VMT) and based the same rheological and damage models ($V = 300 \text{ m}\cdot\text{s}^{-1}$ and $T_0 = 293\text{K}$)

4 Orthogonal Ti6Al4V machining

4.1 Experimental tests

Orthogonal dry turning tests of the Ti6Al4V titanium alloy were performed on the LEADWELL LTC25iL CNC lathe. An uncoated tungsten carbide insert referenced AP40 122002-ARNO, which was fixed on the insert holder, was used. The cylindrical workpiece was previously prepared with bearings of 3 mm width (Fig. 11) in order to reproduce the orthogonal machining configuration. The cutting conditions are grouped in Table 3. Measurements of the instantaneous forces in different directions were done through the Kistler dynamometer. An optical microscope was used for the chip morphology investigation. Properties of the cutting tool geometry are summarized in Table 3.

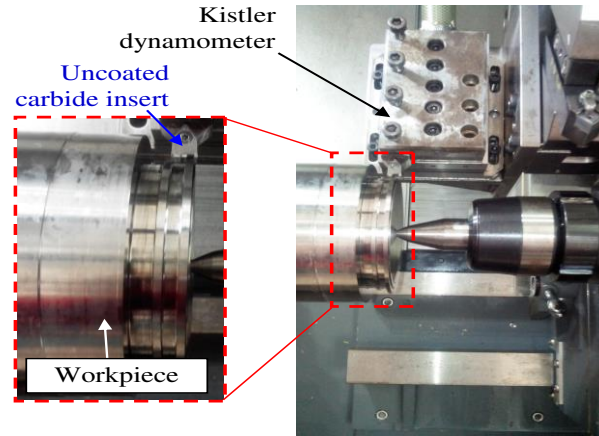


Fig. 11 Experimental device of machining tests

Table 3 Cutting conditions, insert tool geometry and material properties

Cutting conditions	
Cutting speed V_c (m/min)	45 _ 60 _ 75
Uncut chip thickness f (mm)	0.15 _ 0.22 _ 0.3
Width of cut a_p (mm)	3
Tool geometry	
Rake angle γ ($^\circ$)	6
Clearance angle α ($^\circ$)	7
Edge inclination angle λ_s ($^\circ$)	0
Edge entering angle κ_r ($^\circ$)	90
Cutting edge radius r_b (μm)	20
Tool material properties [35]	
Density ρ (kg/m^3)	15000
Specific heat C_p (J/kg/K)	203
Thermal conductivity λ (W/m/K)	46
Thermal expansion α_p ($\mu\text{m.m/K}$)	4.7×10^{-6}

4.2 Numerical modeling

The 3D modeling of orthogonal turning was carried out. An assumption of temperature-displacement coupling conditions was made. The case of explicit and Lagrangian conditions was investigated. A multi-part deformed workpiece was defined for a better control of the mesh distortion, which is involved in the contact interfaces and the shear

zones. The workpiece was conceived in three tied parts: the uncut chip zone (P₁), the chip separation zone corresponding to the cutting tool passage zone (P₂) and the workpiece support (P₃). The model geometry and the boundary conditions are illustrated in Fig. 12. The cutting speed was applied to the rigid tungsten carbide tool, whereas the workpiece was fixed at its bottom side. The 3D 8-node thermally coupled continuum square elements with a reduced integration C3D8RT were used in the model discretization. A mesh refinement was applied in specific zones, where the initial geometry was critical (case of the tool edge radius) and pronounced geometry changes were taking place (P₁ and P₂). The mesh furthest from these zones was the coarsest. This assumption aimed to reduce the computing time (the *CPU* time). The same experimental cutting conditions (see Table 3) were modeled.

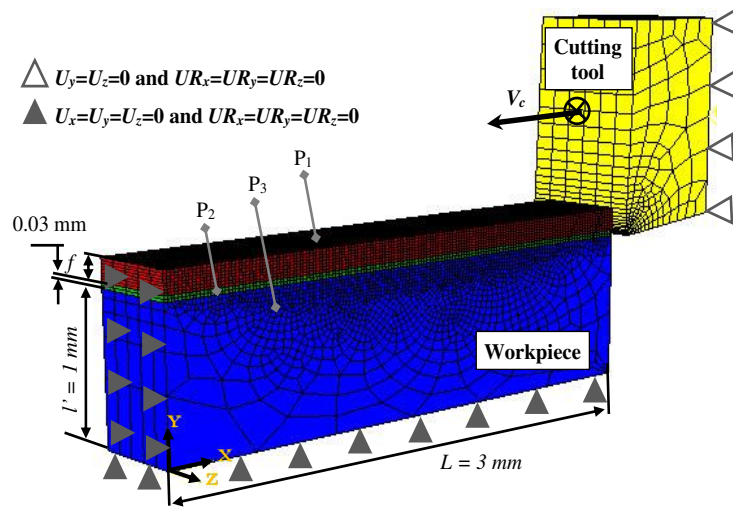


Fig. 12 Numerical model geometry and boundary conditions

In this study, both rheological models, the ‘standard’ JC model [17] and the proposed one given by Eq. (5), were used for the modeling of the Ti6Al4V machining. The damage initiation model [33] and the failure evolution laws (see Eqs. (22) and (23)) were defined in the numerical simulations, in the aim to reproduce the material removal process and the chip segmentation. The Coulomb-Tresca friction model (see Eq. (25)), which has been commonly used in the literature review [3, 7, 21, 36] to model the

machining process, was defined to predict the stick-slip conditions induced in the contact interfaces. In order to model the important thermomechanical coupling conditions following the Ti6Al4V machining and resulting in pronounced heating of the workpiece and the cutting tool, all the energy generated by the friction work was assumed converted to a heat flow. In addition, the case of the conversion of 90% of the workpiece plastic deformation to a thermal energy was considered.

$$\tau_f = \max \left(\mu \times \sigma_n, m_{Tresca} \times \frac{\sigma}{\sqrt{3}} \right) \quad (25)$$

where μ and m_{Tresca} are the Coulomb's friction coefficient and the Tresca factor respectively. $\frac{\sigma}{\sqrt{3}}$ and σ_n are the average shear stress and the normal friction stress, respectively.

4.3 Experimental and numerical results of the Ti6Al4V machining and discussion

4.3.1 Chip segmentation and side burr formation

Fig. 13 illustrates the experimental chip morphology obtained for different cutting speeds and feed rates. For all investigated cutting conditions, the Ti6Al4V machining resulted in the formation of saw-toothed chips. The sensitivity of the chip segmentation, the segment geometry and the crack propagation within the formed shear bands to the machining conditions was underlined. For the lowest cutting speed and feed rate (45 m/min and 0.15 mm/rev, respectively), an irregular chip segmentation was underlined. However, the cutting condition increase gave rise to more pronounced and regular chip serration and more accentuated crack propagation. Quantitative measurements of the peak height (H), the valley height (h) and the segment width (L_s) of experimental chips were made. Fig. 14 illustrates a low sensitivity of the chip geometry to the cutting speeds, which was not

the case of the feed rate. The H and L_s mean values were almost doubled when the feed rates was increased from 0.15 mm/rev to 0.3 mm/rev resulting in more pronounced chip segmentation. However, lower effects of the f value on the valley height was noted, since only variations about 17% of the average computed h were underlined for all investigated cutting speeds.

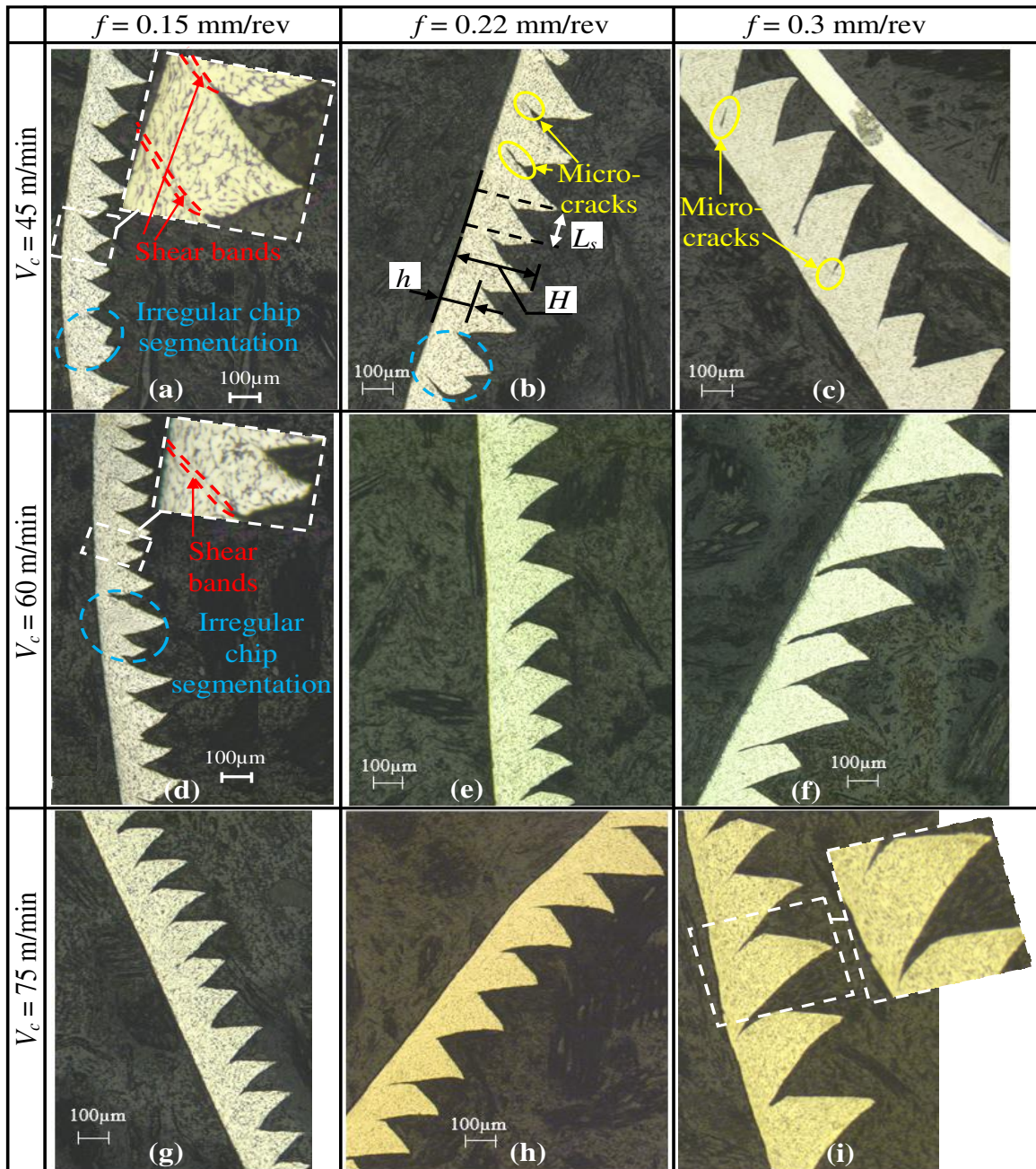


Fig. 13 Experimental chip morphologies corresponding to different cutting conditions

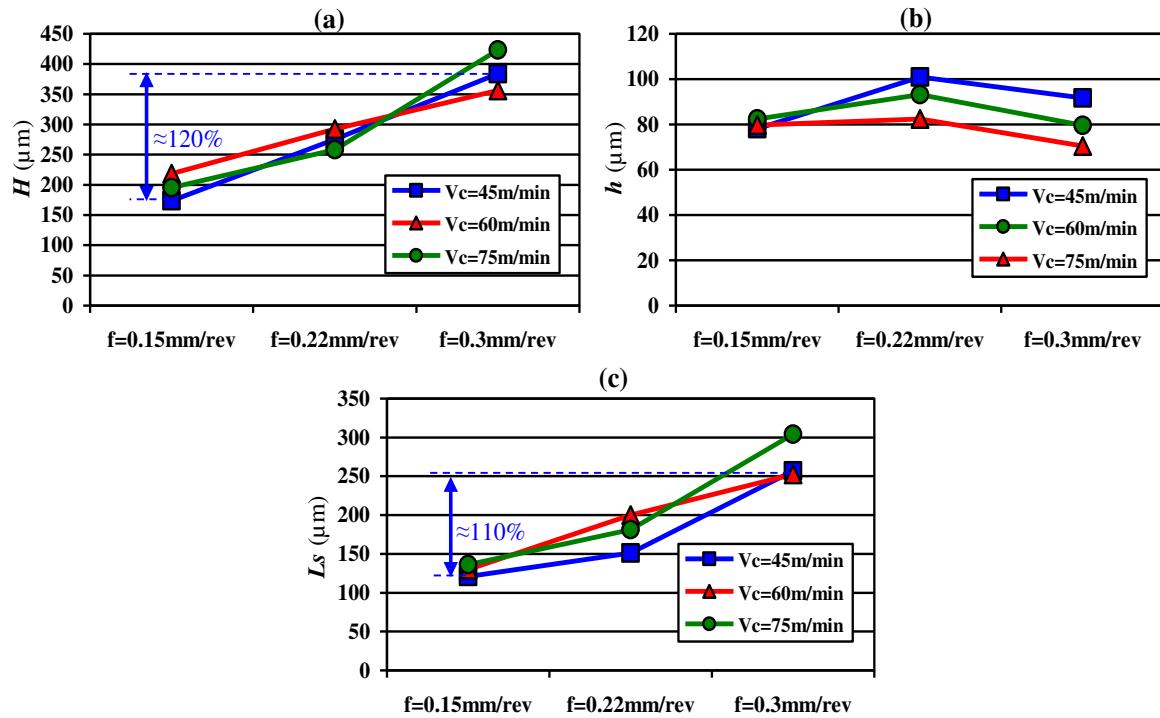


Fig. 14 Experimental average (a) peak height, (b) valley height and (c) segments width for different cutting conditions

The numerical chips predicted with the JC rheological model and the proposed one (see Eq. (5)) were compared to the experimental ones obtained for the same cutting conditions. The adequacy of both models in terms of accurately predicting the machining process of the Ti6Al4V titanium alloy was investigated. In correlation with the experimental chip morphology, the lowest segmentation was modeled when a cutting speed and a feed rate of 45 m/min and 0.15 mm/rev, respectively, were defined (see Fig. 15). For $f = 0.15$ mm/rev, a wavy to slightly segmented chip was predicted with the empirical JC model definition, whatever the cutting speed value, which was in a mismatch with the experimental results. However, more serrated chip was simulated for the same cutting conditions, when the proposed rheological model was used to predict the workpiece material behavior.

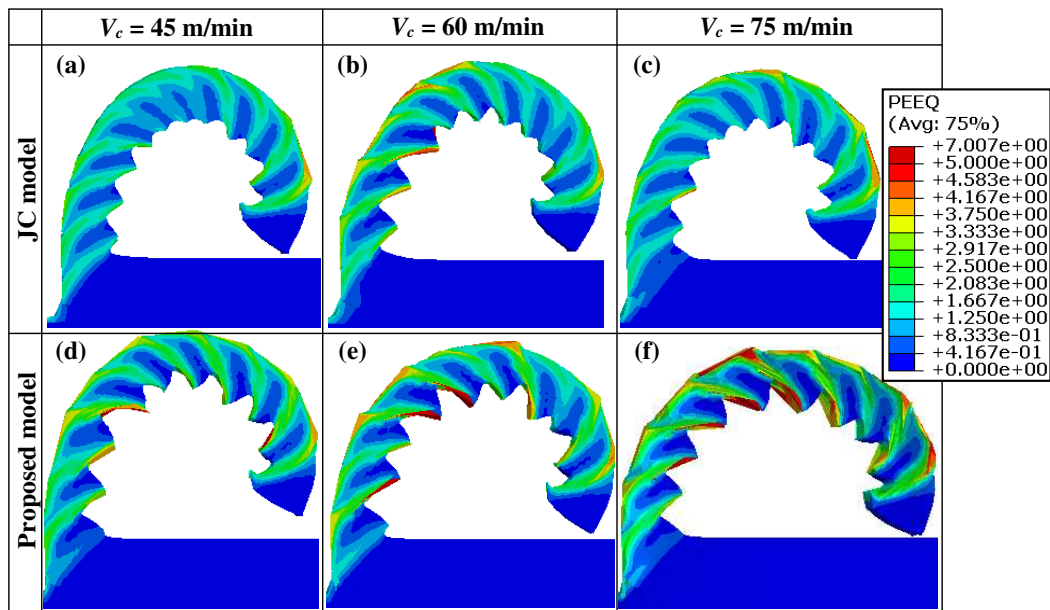


Fig. 15 Numerical chip morphology predicted with (a-c) the JC and (d-f) the proposed rheological models and corresponding to different cutting speeds ($f = 0.15 \text{ mm/rev}$)

Comparisons with the experimental chips obtained for higher feed rates (0.22 mm/rev and 0.3 mm/rev) underlined the inability of the JC empirical model to adequately predict the Ti6Al4V alloy behavior. Even though a slight increase of the chip serration intensity with the cutting speed was enabled with this model, Fig. 16 and Fig. 17 show the modeling of weakly segmented chips for feed rates of 0.22 mm/rev and 0.3 mm/rev, which was in a mismatch with the real chip morphology. Contrariwise, the accentuation of the chip segmentation with the cutting speed and the feed rate increase was accurately predicted with the proposed rheological model. For all investigated cutting conditions, numerical chips in correlation with the experimental ones were modeled. This new constitutive model enabled a suitable prediction of the pronounced effect of the feed rate on the chip morphology. Very serrated chips with pronounced equivalent plastic strains were modeled in the well-formed shear bands, for the highest feed rate.

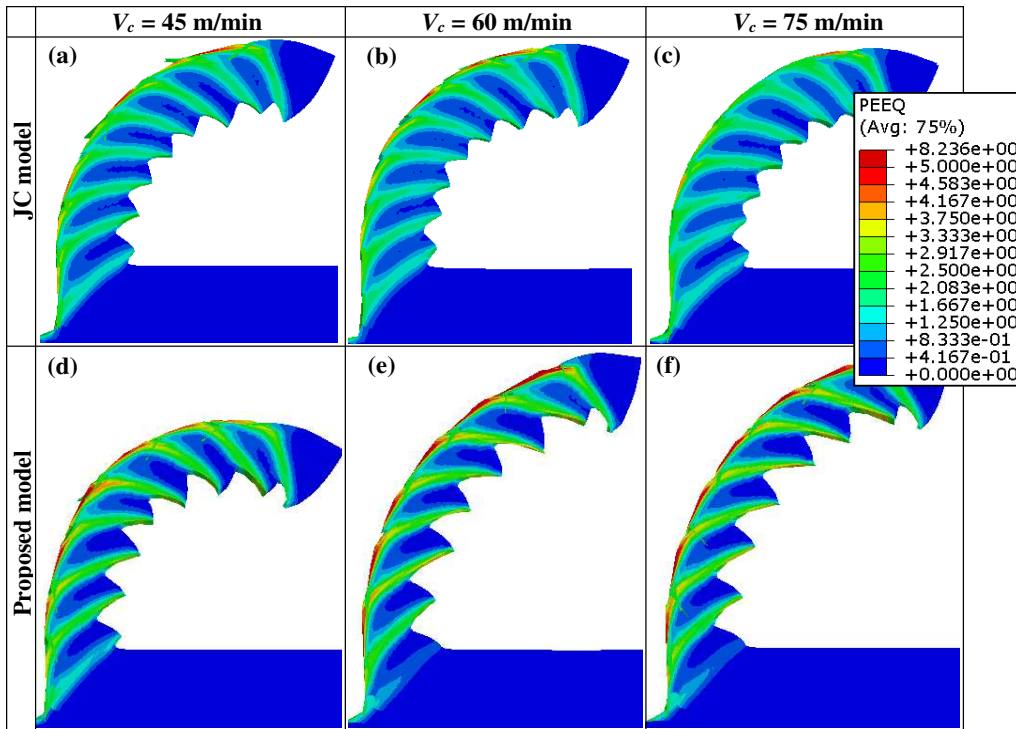


Fig. 16 Numerical chip morphology modeled with different rheological models for several cutting speeds ($f = 0.22 \text{ mm/rev}$)

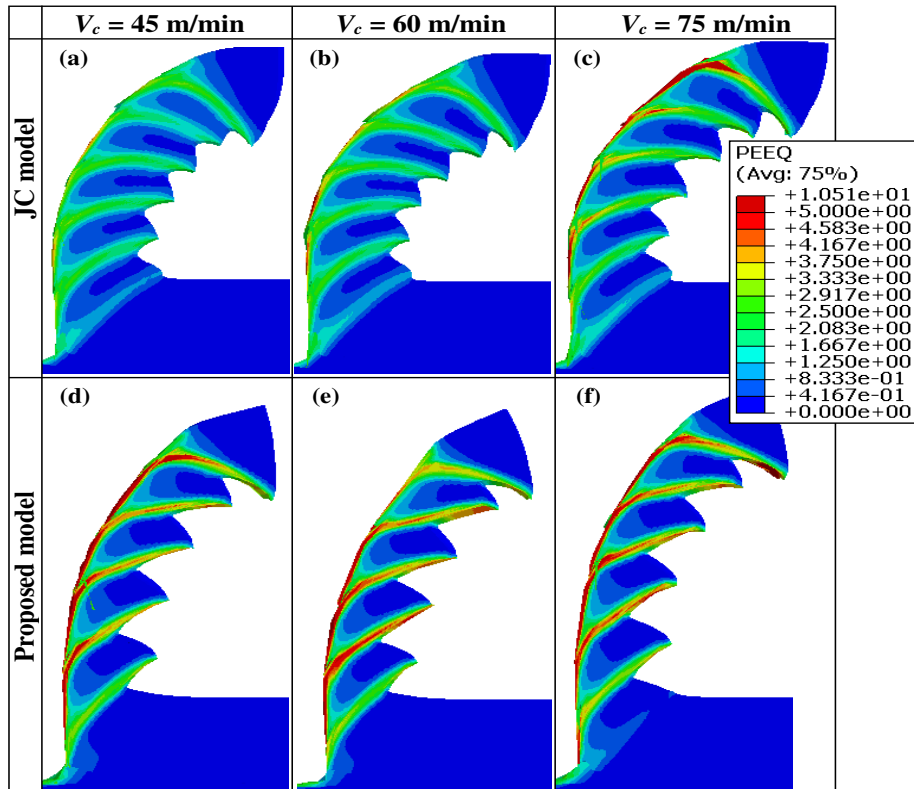


Fig. 17 Numerical chip morphology for a feed rate of 0.3 mm/rev and different cutting speeds: (a-c) JC and (d-f) proposed rheological models

Quantitative comparisons of the chip geometry were carried out to investigate the reliability of proposed phenomenological model. The computed peak and valley heights of numerical chips predicted with both models, the ‘standard’ JC model and the proposed one, were determined. The segmentation ratio SR of experimental and numerical chips were determined and compared (see Eq. (26)). It is underlined that the SR increase corresponds to a more segmented chip. For all investigated cutting conditions, SR very close to the experimental ones were predicted with the proposed model (see Fig. 18). The sensitivity of the experimental chip geometry to the cutting speed and the feed rate was adequately modeled. Maximum errors of 15% were obtained, while pronounced mismatched chip valley and peak heights were predicted with the JC rheological model mainly for the highest feed rates. In the case of $f = 0.3$ mm/rev, errors up to 83% were determined (see Fig. 18).

$$SR(\%) = 100 \times \left(\frac{H - h}{H} \right) \quad (26)$$

where h and H are the valley and the peak chip heights, respectively.

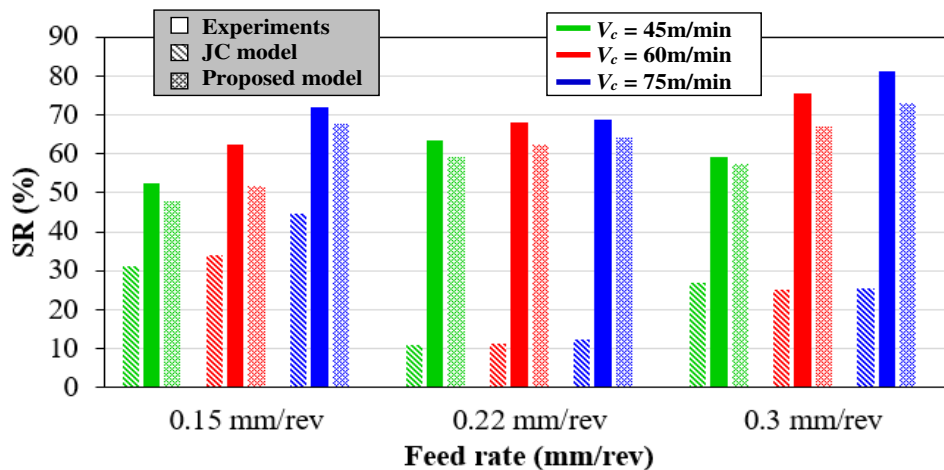


Fig. 18 Comparison of experimental and numerical segmentation ratio for different cutting conditions

The comparisons of numerical chips to the experimental ones underlined the advantageous of the modified JC model. It enabled the accurate prediction of the chip morphology and the segments geometry, mainly in the case of high-feed rates. For these

cutting conditions, the efficiency of the 3D FE modeling in taking into account the effects of the material flow in the cutting direction, as well as in the width of cut direction, on the machining process was underlined. For all investigated cutting conditions, side burrs were predicted in the numerical chips (see Fig. 19). A low sensitivity of its average width w_{sb} to the cutting speed was noted. Contrariwise, the definition of important feed rates gave rise to a significant material flow in the side edges of the workpiece, which influenced the machining process in terms of the cutting forces applied to the cutting tool, the temperature distribution in both materials, the contact conditions and the tool wear. For a cutting speed of 75 m/min, w_{sb} increased from 0.072 μm to almost 0.15 μm when feed rates of 0.15 mm/rev and 0.3 mm/rev were modeled, respectively. The modeling of side burrs was not permitted with 2D numerical simulations pointing out the advantageous of 3D modeling, even in the case of orthogonal machining.

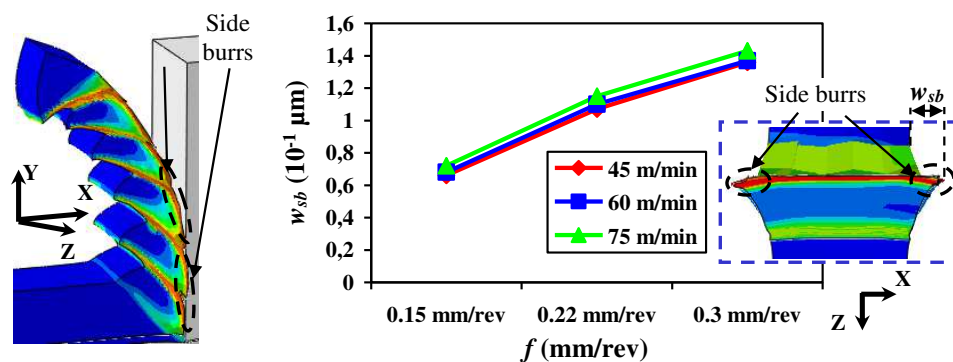


Fig. 19 Side burrs width corresponding to different cutting conditions

4.3.2 Cutting forces

The effect of the cutting conditions on the instantaneous forces applied to the cutting tool was investigated. Measurements of the cutting and the feed forces were carried out once the established regime was reached. In general, more sensitivity of the experimental forces to the feed rate was underlined (see Fig. 20). Due to the definition of the highest feed rate, the penetration of the cutting tool in the workpiece and its displacement was followed by a significant increase of the quantity of the machined material. Therefore,

higher cutting and feed forces were obtained during the Ti6Al4V machining. Nonetheless, Fig. 21 shows a low sensitivity of the experimental cutting forces to the cutting speed. For all studied feed rates, F_c was slightly decreased with the V_c increase due to the temperature rise in the contact interfaces and the shear bands. It resulted in more pronounced softening of the machined material, which was easier to remove. However, a F_f rise with the cutting speed increase was noted (Fig. 21-b).

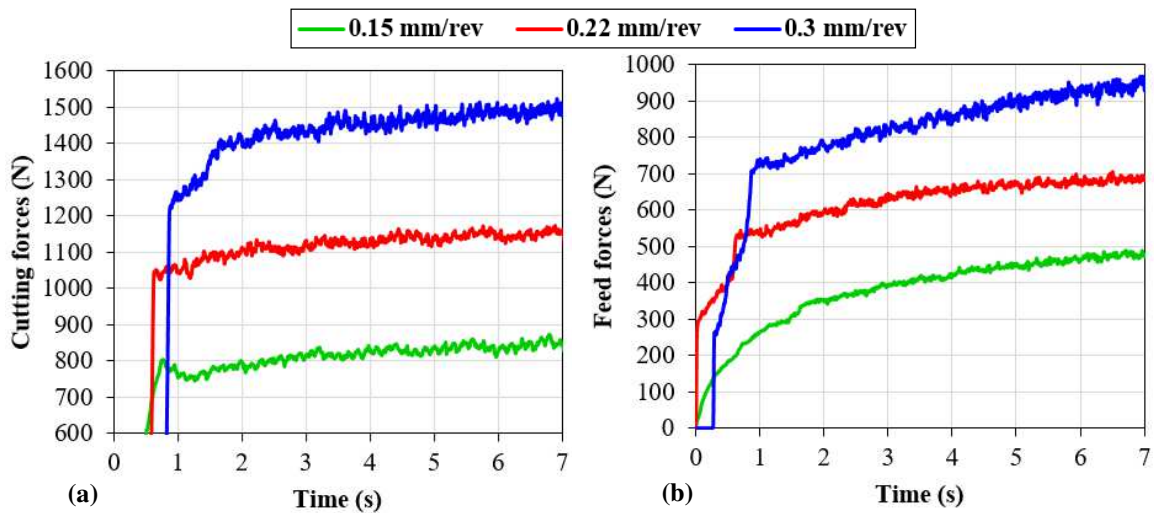


Fig. 20 Experimental forces corresponding to different feed rates ($V_c = 45$ m/min): (a) cutting and (b) feed forces

Comparisons of experimental and numerical cutting forces for all investigated cutting conditions were set up (see Fig. 22). Its low sensitivity to the cutting speed was accurately predicted with both compared rheological models. For a feed rate of 0.15 mm/rev, numerical cutting forces were generally close to the experimental ones. Errors below 10% were computed. The important sensitivity of the F_c mean value to the feed rate was reliably reproduced in the case of the new constitutive model definition. However, very mismatched results were predicted by the JC thermo-visco-plastic model, for the highest feed rates. Errors up to 31% were reached, while it was ranged between 0.08% and 0.9% in the case of the proposed model definition. It allowed high agreements with the experimental results for all investigated cutting conditions. A more reliable FE

modeling of the Ti6Al4V orthogonal machining was ensured, even for high feed rates, which was not the case of the ‘standard’ JC model. It enabled more accurate predictions of the strain rate and the temperature effects on the Ti6Al4V behavior without increasing the identification cost of the constitutive coefficients.

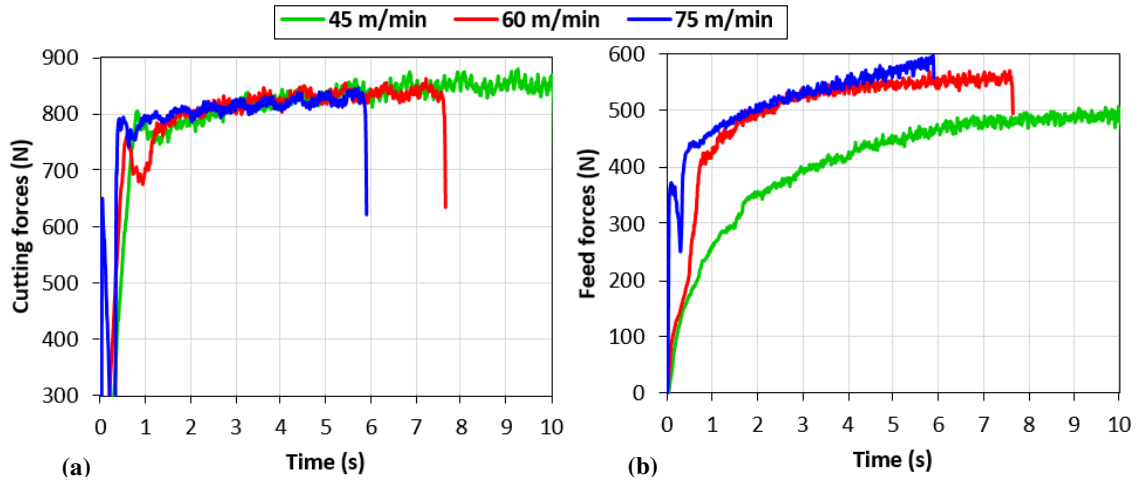


Fig. 21 Experimental (a) cutting and (b) feed forces obtained for different cutting speeds ($f = 0.15$ mm/rev)

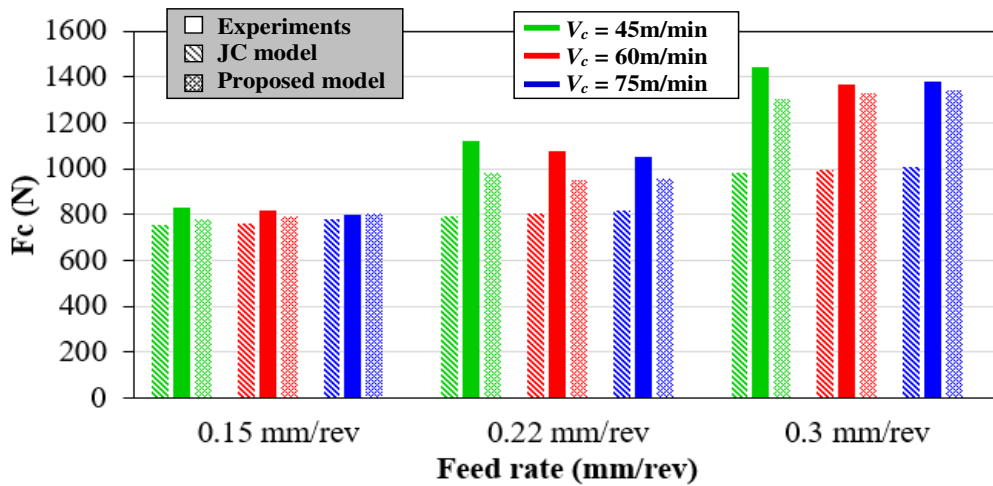


Fig. 22 Mean experimental and numerical cutting forces corresponding to different cutting conditions

5 Conclusion

In this study, a new phenomenological model was proposed. It was used to predict the Ti6Al4V titanium alloy behavior in the case of uniaxial compression test and cutting

process, for several loading conditions. Its ability to overcome the weaknesses of the JC thermo-visco-plastic law, mainly summarized on its limited validity to particular ranges of strain rate and temperature, was exhibited. An enhanced prediction of the experimental material behavior was ensured for all studied material forming tests. Computed stress-strain curves close to the real ones were modeled. In addition, the identification of its constitutive coefficients was done without setting up specific or additional experimental tests. An interesting compromise between the identification cost and the numerical model accuracy was guaranteed with this rheological model.

The implementation of the proposed rheological model in the FE code Abaqus®/Explicit was done. For the VUMAT validation, comparisons of the numerical results directly predicted with the constitutive and damage models, which are already implemented in the FE code Abaqus®, to those modeled with the subroutine and corresponding to the definition of the same models. The numerical simulations of uniaxial tensile tests and axisymmetric impact tests pointed out the robustness of the subroutine, for several loading conditions.

The 3D modeling of orthogonal cutting process was done, for different cutting speeds and feed rates. The efficiency of the JC rheological model and the proposed one was compared. Comparisons were set up with the experimental results of the orthogonal machining tests. Despite the modeling of the same cutting conditions, different chip segmentation intensity and cutting forces were predicted. The FE analysis reliability was increased due to the definition of the proposed constitutive model to the workpiece material, which pointed out its adequacy in accurately predicting the Ti6Al4V alloy behavior under wide ranges of plastic strain, strain rate and temperature. The effect of the cutting conditions on the chip segmentation, the serration ratio and the cutting forces were

adequately predicted. Contrariwise, mismatched numerical results were modeled with the JC empirical model, mainly for important feed rates (of 0.22 mm/rev and 0.3 mm/rev).

Nonetheless, the advantageous of 3D numerical simulations in the case of the machining process investigation were underlined. The definition of high feed rates gave rise to very pronounced material flow along the width of cut direction. The modeled side burr, which width increased due to the feed rate rise, resulted in additional thermomechanical loads. The effects of the formed side burrs on the cutting tool were neglected with the 2D FE modeling, emphasizing consequently its inadequacy, even in the case of orthogonal cutting conditions. Although the most important material flow was at the chip thickness level, taking into account the phenomena induced towards the width of cut direction, from the workpiece median plane to its side edges, was also required for more reliable prediction of the machining process.

In conclusion, this study pointed out the effect of the proposed rheological model on allowing more suitable predictions of the workpiece material behavior, for several loading conditions, while maintaining a low cost of the constitutive coefficients identification. In addition, a more reliable modeling of the Ti6Al4V machining process was ensured when it was coupled with 3D numerical simulations.

Acknowledgments

The authors gratefully acknowledge the financial support provided for this work by Arts et Métiers _ Campus d'Angers, France, especially the PMD team, and the National School of Engineers of Sfax, Tunisia.

Declarations

Funding This study was funded by Arts et Métiers _ Campus d'Angers, France and the National School of Engineers of Sfax, Tunisia

Conflicts of Interest / Competing Interests The authors have no conflicts of interest to declare that are relevant to the content of this article

Availability of data and materials The data presented and analyzed in this study are available from the corresponding author on reasonable request.

Code availability The code used in this study is available from the corresponding author on reasonable request.

Ethics approval Not applicable

Consent to participate Not applicable

Consent for publication All authors consent to the publication of this research work.

References

1. Veiga C, Paulo Davim J, Loureiro AJR (2013) Review on machinability of titanium alloys: The process perspective. *Rev Adv Mater Sci* 34:148–164. <https://doi.org/10.3945/jn.109.108399>
2. Arrazola PJ, Garay A, Iriarte LM, et al (2009) Machinability of titanium alloys (Ti6Al4V and Ti555.3). *J Mater Process Technol* 209:2223–2230. <https://doi.org/10.1016/j.jmatprotec.2008.06.020>
3. Harzallah M, Pottier T, Senatore J, et al (2017) Numerical and experimental investigations of Ti-6Al-4V chip generation and thermo-mechanical couplings in orthogonal cutting. *Int J Mech Sci* 134:189–202. <https://doi.org/10.1016/j.ijmecsci.2017.10.017>
4. Pottier T, Germain G, Calamaz M, et al (2014) Sub-Millimeter Measurement of Finite Strains at Cutting Tool Tip Vicinity. *Exp Mech* 54:1031–1042. <https://doi.org/10.1007/s11340-014-9868-0>
5. Ali MH, Ansari MNM, Khidhir BA, et al (2014) Simulation machining of titanium alloy (Ti-6Al-4V) based on the finite element modeling. *J Brazilian Soc Mech Sci Eng* 36:315–324. <https://doi.org/10.1007/s40430-013-0084-0>
6. Arrazola PJ, Barbero O, Urresti I (2010) Influence of material parameters on serrated chip prediction in finite element modeling of chip formation process. *Int J Mater Form* 3:519–522. <https://doi.org/10.1007/s12289-010-0821-1>

7. Yaich M, Ayed Y, Bouaziz Z, Germain G (2017) Numerical analysis of constitutive coefficients effects on FE simulation of the 2D orthogonal cutting process: application to the Ti6Al4V. *Int J Adv Manuf Technol* 93:283–303. <https://doi.org/10.1007/s00170-016-8934-4>
8. Biermann D, Höhne F, Sieben B, Zabel A (2010) Finite element modeling and three-dimensional simulation of the turning process incorporating the material hardness. *Int J Mater Form* 3:459–462. <https://doi.org/10.1007/s12289-010-0806-0>
9. Franchi R, Del Prete A, Umbrello D (2017) Inverse analysis procedure to determine flow stress and friction data for finite element modeling of machining. *Int J Mater Form* 10:685–695. <https://doi.org/10.1007/s12289-016-1311-x>
10. Haddag B, Atlati S, Nouari M, Znasni M (2010) Finite element formulation effect in three-dimensional modeling of a chip formation during machining. *Int J Mater Form* 3:527–530. <https://doi.org/10.1007/s12289-010-0823-z>
11. Rizzuti S, Umbrello D, Filice L, Settineri L (2010) Finite element analysis of residual stresses in machining. *Int J Mater Form* 3:431–434. <https://doi.org/10.1007/s12289-010-0799-8>
12. Parida AK, Maity K (2017) Effect of nose radius on forces, and process parameters in hot machining of Inconel 718 using finite element analysis. *Eng Sci Technol an Int J* 20:687–693. <https://doi.org/10.1016/j.jestch.2016.10.006>
13. Lurdos O (2008) Lois de comportement et recristallisation dynamique : approches empirique et physique. Ecole Nationale Supérieure des Mines _ Saint-Etienne
14. Hor A (2011) Simulation physique des conditions thermiques de forgeage et d'usinage-Caractérisation et modélisation de la rhéologie et de l'endommagement. École Nationale Supérieure d'Arts et Métiers_Campus d'Agers
15. Ayed Y (2013) Approches expérimentales et numériques de l'usinage assisté jet d'eau haute pression : étude des mécanismes d'usure et contribution à la modélisation multi-physiques de la coupe. Thèse
16. Hor A, Morel F, Lebrun JL, Germain G (2013) Modelling, identification and application of phenomenological constitutive laws over a large strain rate and temperature range. *Mech Mater* 64:91–110. <https://doi.org/10.1016/j.mechmat.2013.05.002>

17. Johnson GR, Cook WH (1983) A constitutive model and data for metals subjected to large strains, high strain rates and high temperatures. Proc. 7th Int. Symp. Ballist. 547:541–547
18. Saleem W, Asad M, Zain-ul-abdein M, et al (2016) Numerical investigations of optimum turning parameters—AA2024-T351 aluminum alloy. Mach Sci Technol 20:634–654. <https://doi.org/10.1080/10910344.2016.1224019>
19. Molinari A, Cheriguene R, Miguelez H (2012) Contact variables and thermal effects at the tool-chip interface in orthogonal cutting. Int J Solids Struct 49:3774–3796. <https://doi.org/10.1016/j.ijsolstr.2012.08.013>
20. Zhang YC, Mabrouki T, Nelias D, Gong YD (2011) Chip formation in orthogonal cutting considering interface limiting shear stress and damage evolution based on fracture energy approach. Finite Elem Anal Des 47:850–863. <https://doi.org/10.1016/j.finel.2011.02.016>
21. Yaich M, Ayed Y, Bouaziz Z, Germain G (2020) A 2D finite element analysis of the effect of numerical parameters on the reliability of Ti6Al4V machining modeling. Mach Sci Technol 24:509–543. <https://doi.org/10.1080/10910344.2019.1698606>
22. Ludwik P (1909) Elemente der technologischen Mechanik
23. Ayed Y, Germain G, Ammar A, Furet B (2017) Thermo-mechanical characterization of the Ti17 titanium alloy under extreme loading conditions. Int J Adv Manuf Technol 90:1593–1603. <https://doi.org/10.1007/s00170-016-9476-5>
24. Gavrus A (2012) Constitutive Equation for Description of Metallic Materials Behavior during Static and Dynamic Loadings Taking into Account Important Gradients of Plastic Deformation. Key Eng Mater 504–506:697–702. <https://doi.org/10.4028/www.scientific.net/kem.504-506.697>
25. Liu S, Kouadri-Henni A, Gavrus A (2018) DP600 dual phase steel thermo-elasto-plastic constitutive model considering strain rate and temperature influence on FEM residual stress analysis of laser welding. J Manuf Process 35:407–419. <https://doi.org/10.1016/j.jmapro.2018.07.006>
26. Braham-Bouchnak T (2010) Etude du comportement en sollicitations extrêmes et de l'usinabilité d'un nouvel alliage de titane aéronautique: Le Ti555-3. Ecole Nationale Supérieure d'Arts et Métiers-Centre d'Angers

27. Germain G, Morel A, Braham-Bouchnak T (2013) Identification of Material Constitutive Laws Representative of Machining Conditions for Two Titanium Alloys: Ti6Al4V and Ti555-3. *J Eng Mater Technol* 135:. <https://doi.org/10.1115/1.4023674>
28. Chattonjai P (2016) Numerical Implementation of Energy-based Models in Explicit Finite Element Analysis for Sand in Plane Strain Compression. *KMUTNB Int J Appl Sci Technol* 9:53–60. <https://doi.org/10.14416/j.ijast.2016.01.001>
29. Xu S, Guo YF, Ngan AHW (2013) A molecular dynamics study on the orientation, size, and dislocation confinement effects on the plastic deformation of Al nanopillars. *Int J Plast* 43:116–127. <https://doi.org/10.1016/j.ijplas.2012.11.002>
30. Balogh L, Brown DW, Mosbrucker P, et al (2012) Dislocation structure evolution induced by irradiation and plastic deformation in the Zr-2.5Nb nuclear structural material determined by neutron diffraction line profile analysis. *Acta Mater* 60:5567–5577. <https://doi.org/10.1016/j.actamat.2012.06.062>
31. Yang Y, Liu B (2013) Experimental study on formation characteristics and laws of dislocation and stacking fault during cutting of titanium alloy. *Adv Mater Sci Eng*. <https://doi.org/10.1155/2013/306728>
32. Pipard J-M (2012) Modélisation du comportement élasto-viscoplastique des aciers multiphasés pour la simulation de leur mise en forme. *École Nationale Supérieure d'Arts et Métiers_Metz*
33. Johnson GR, Cook WH (1985) Fracture characteristics of three metals subjected to various strains, strain rates, temperatures and pressures. *Eng Fract Mech* 21:31–48
34. Johnson GR, Holmquist T (1989) Test data and computational strengthen and fracture model constants for 23 materials subjected to large strain, high strain rate, and high temperature
35. Ducobu F, Rivière-Lorphèvre E, Filippi E (2016) Material constitutive model and chip separation criterion influence on the modeling of Ti6Al4V machining with experimental validation in strictly orthogonal cutting condition. *Int J Mech Sci* 107:136–149. <https://doi.org/10.1016/j.ijmecsci.2016.01.008>
36. Zhang XP, Shivpuri R, Srivastava AK (2014) Role of phase transformation in chip segmentation during high speed machining of dual phase titanium alloys. *J Mater*

Process Technol 214:3048–3066. <https://doi.org/10.1016/j.jmatprotec.2014.07.007>

Figures

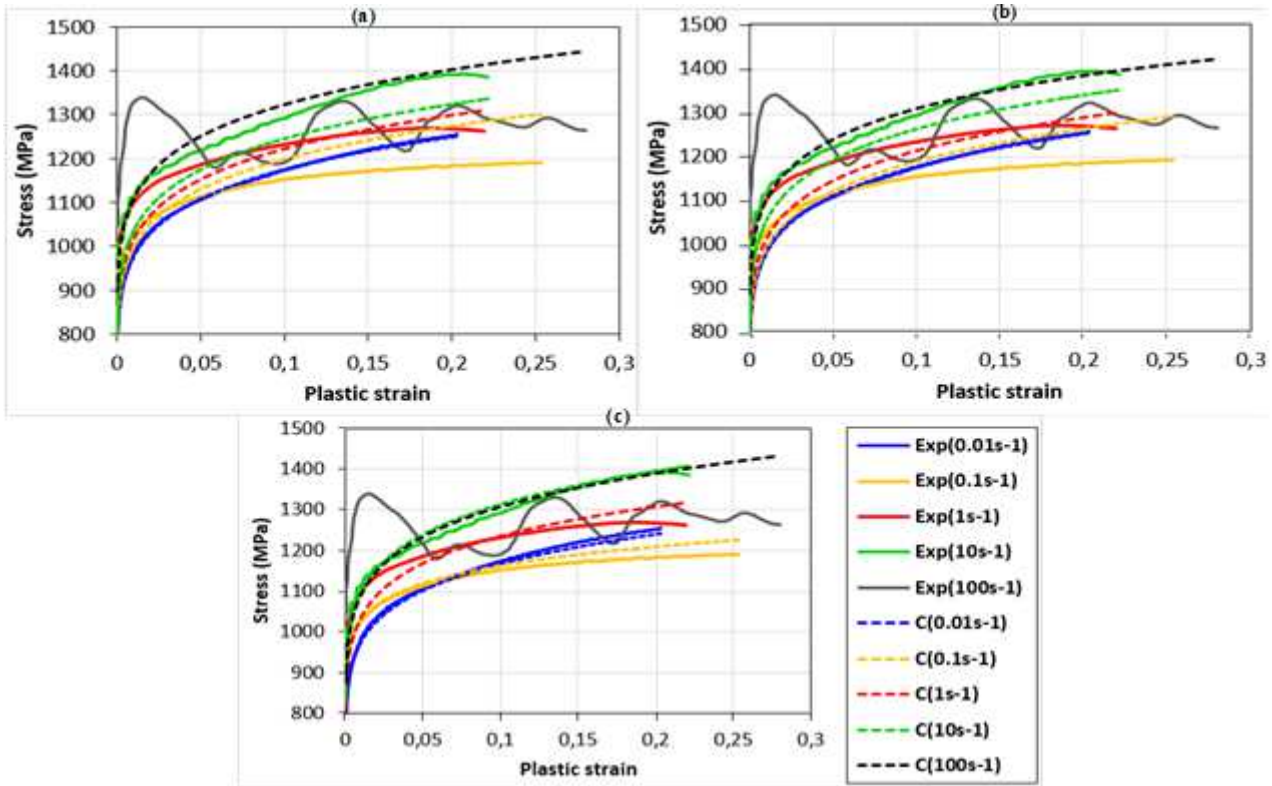


Figure 1

Comparison of the experimental true stress-plastic strain curves obtained for different strain rates and the room temperature to those computed with different rheological models: (a) JC, (b) MJC1 and (c) MJC2 models

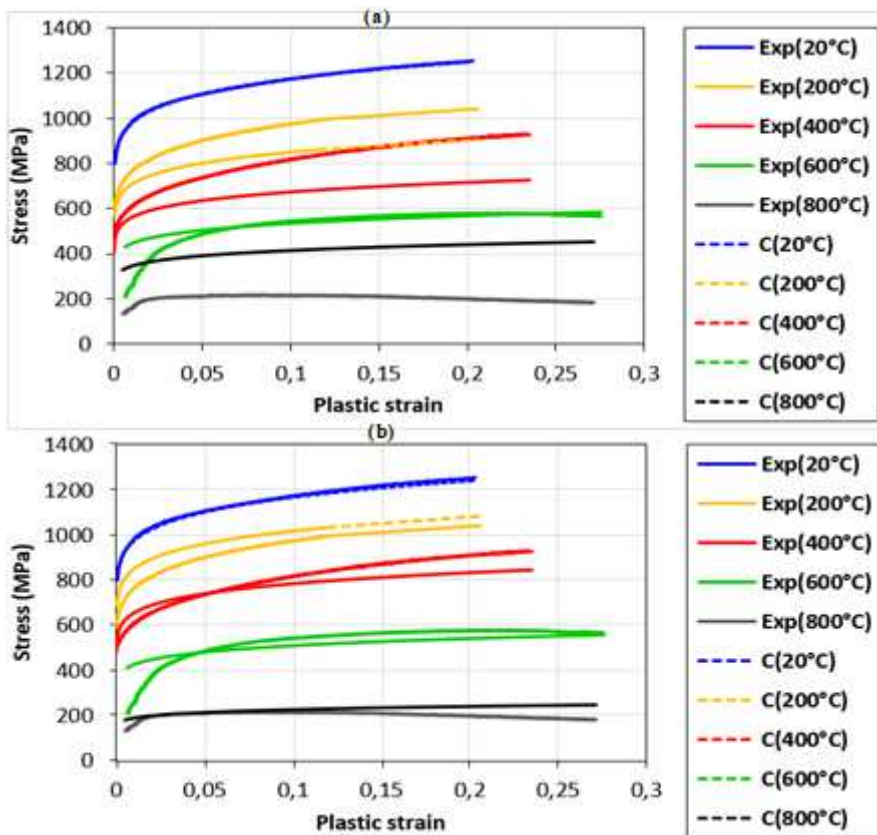


Figure 2

Experimental and computed stress-plastic strain curves corresponding to different initial temperatures and a reference strain rate of 0.01s⁻¹: (a) JC and (b) MJC2 models

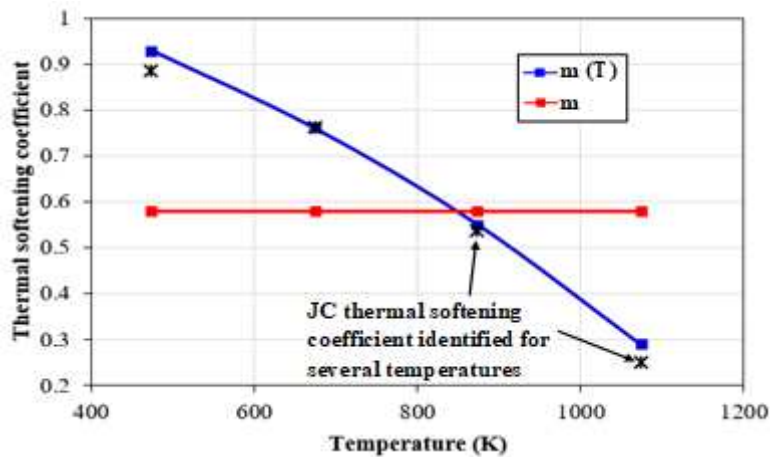


Figure 3

Comparison of the JC thermal softening coefficient to the proposed $m(T)$ function

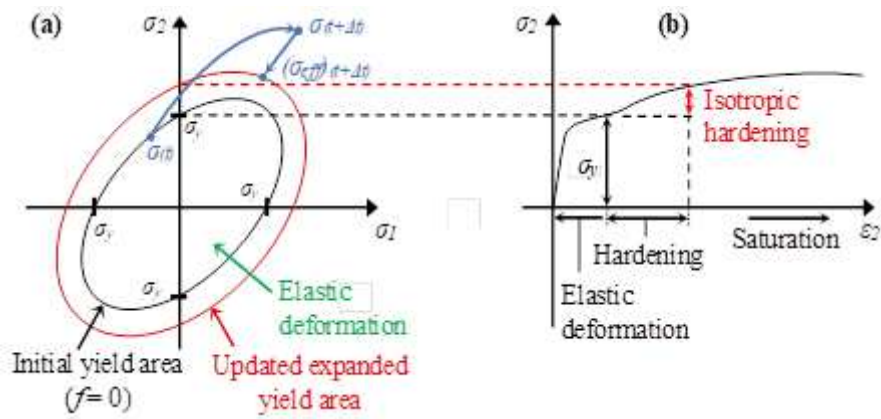


Figure 4

Schematic representation of (a) yield areas in the plane stress and (b) the uniaxial stress-strain curves (case of an isotropic hardening plasticity)

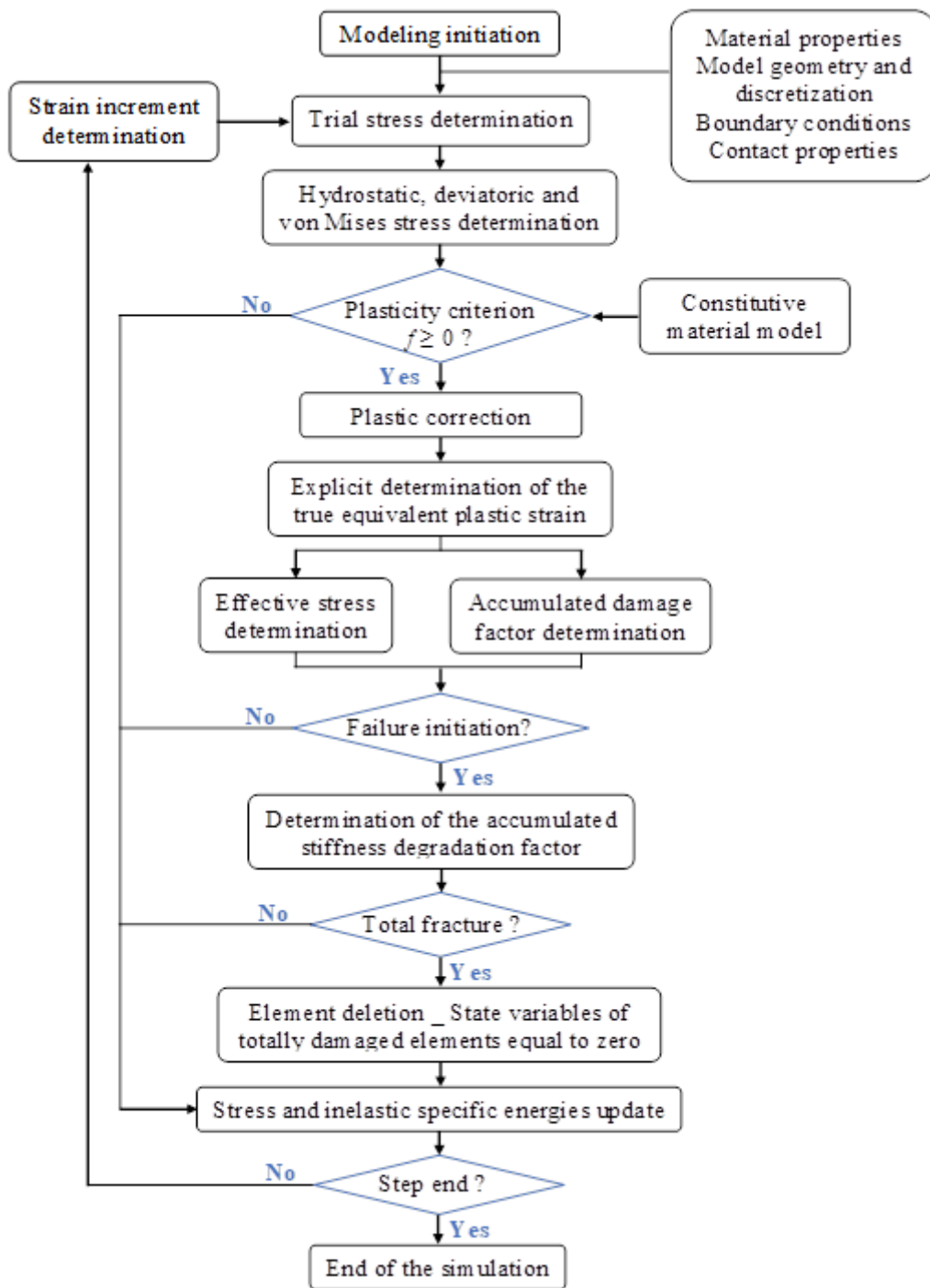


Figure 5

Flowchart of the VUMAT set up to implement the constitutive models in FE software Abaqus®/Explicit

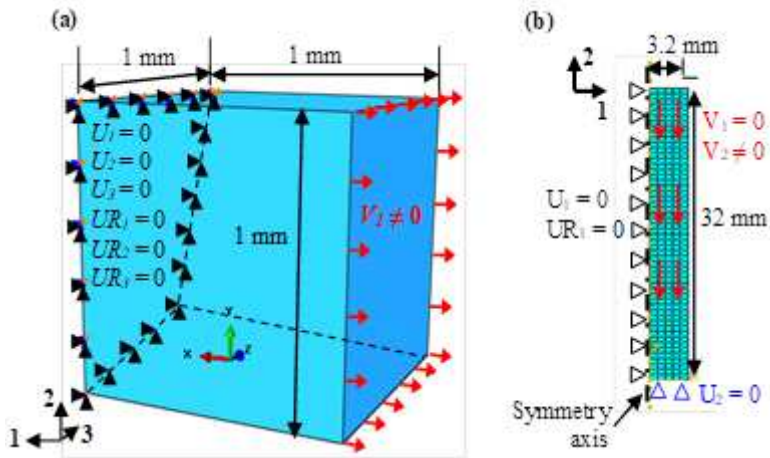


Figure 6

Model geometry and boundary conditions of (a) the 3D tensile test and (b) the 2D axisymmetric impact test

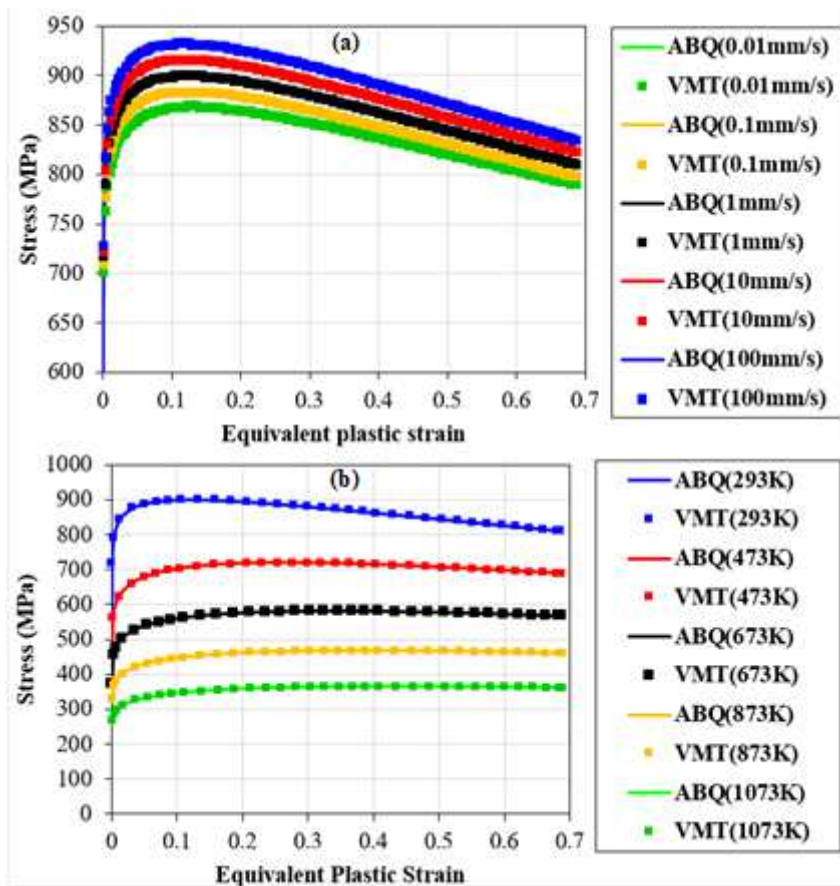


Figure 7

Numerical stress-plastic strain curves predicted when the empirical JC model of the Abaqus® library (ABQ) or that implemented in the VUMAT (VMT) was defined: (a) $T_0 = 293\text{ K}$ and (b) $V = 1\text{ mm/s}$

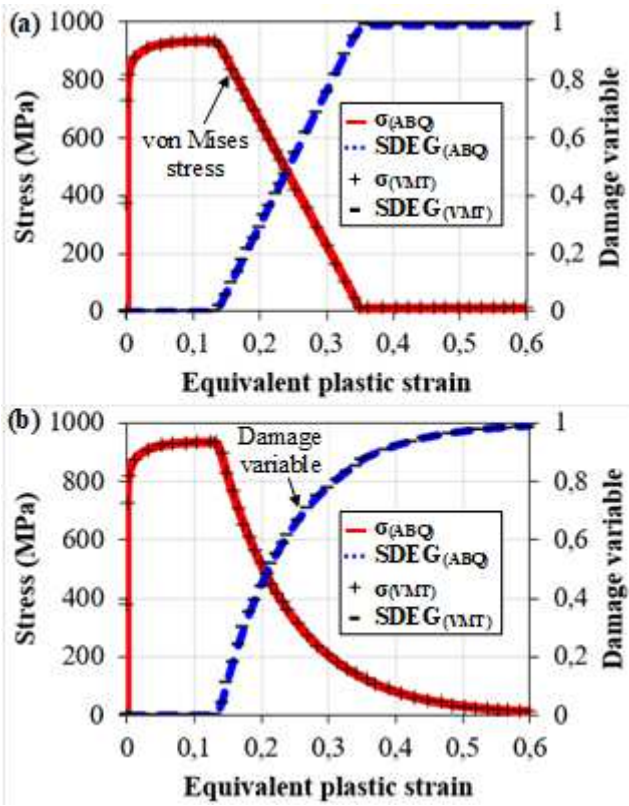


Figure 8

Instantaneous Von Mises stress and damage variable (SDEG) : (a) linear and (b) exponential failure evolution models

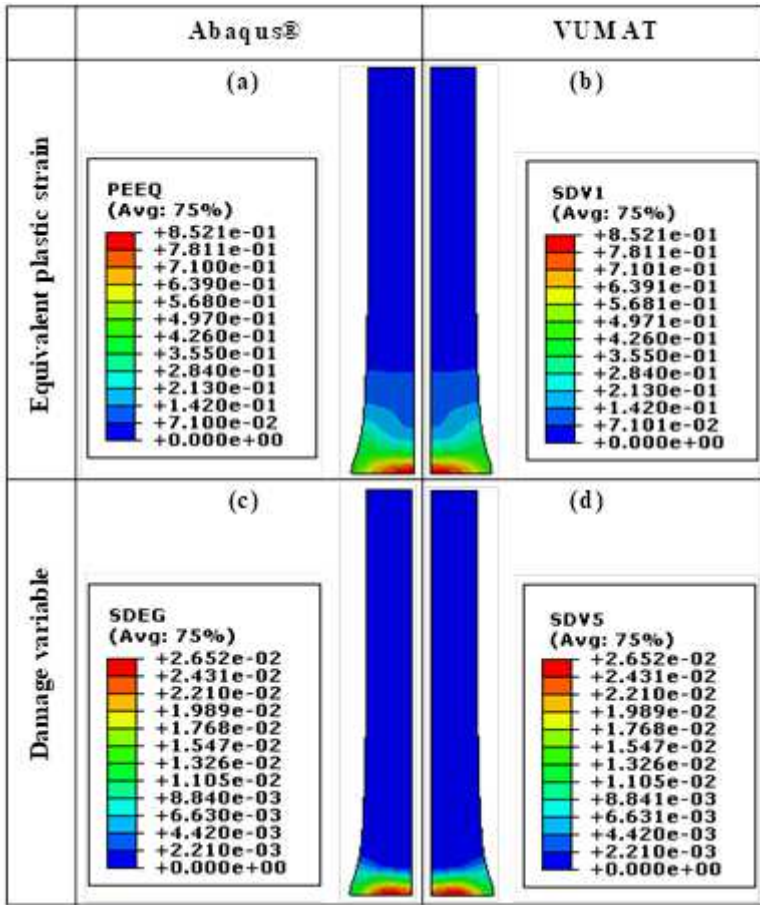


Figure 9

Numerical deformed projectile predicted with (a, c) Abaqus® and (b, d) through the VUMAT definition ($V = 200 \text{ m.s}^{-1}$ and $T_0 = 293\text{K}$): (a-b) Equivalent plastic strain (c-d) and damage evolution variable

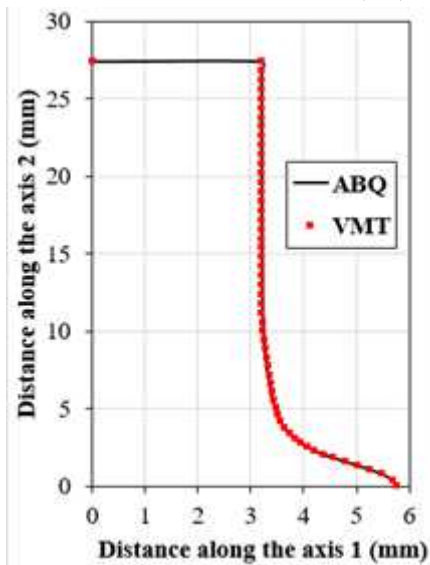


Figure 10

Deformed projectile geometry directly modeled with Abaqus® (ABQ) or through the VUMAT definition (VMT) and based the same rheological and damage models ($V = 300 \text{ m.s}^{-1}$ and $T_0 = 293\text{K}$)

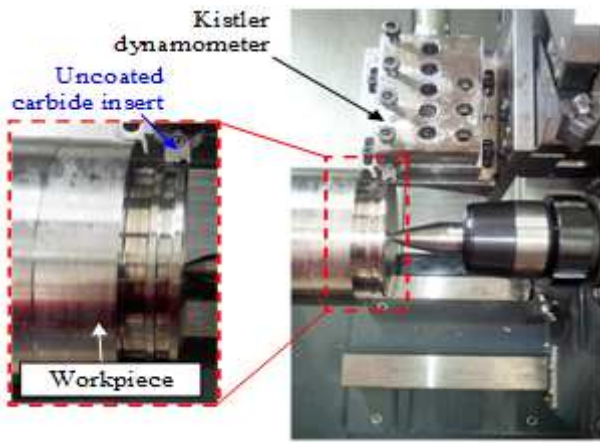


Figure 11

Experimental device of machining tests

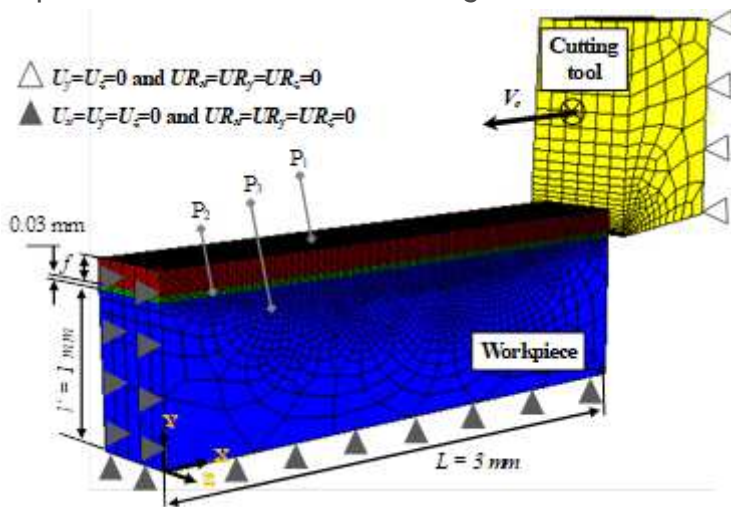


Figure 12

Numerical model geometry and boundary conditions

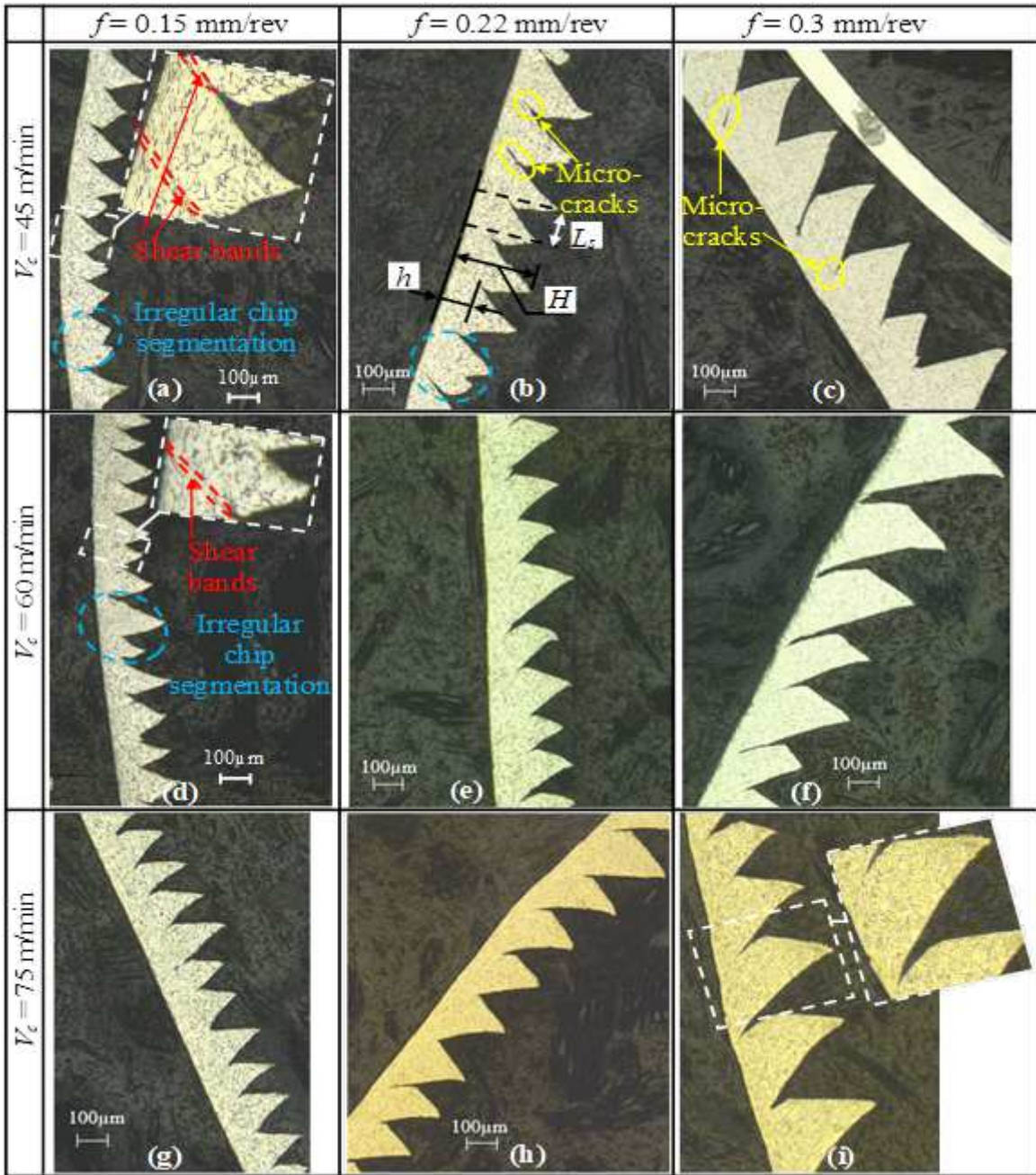


Figure 13

Experimental chip morphologies corresponding to different cutting conditions

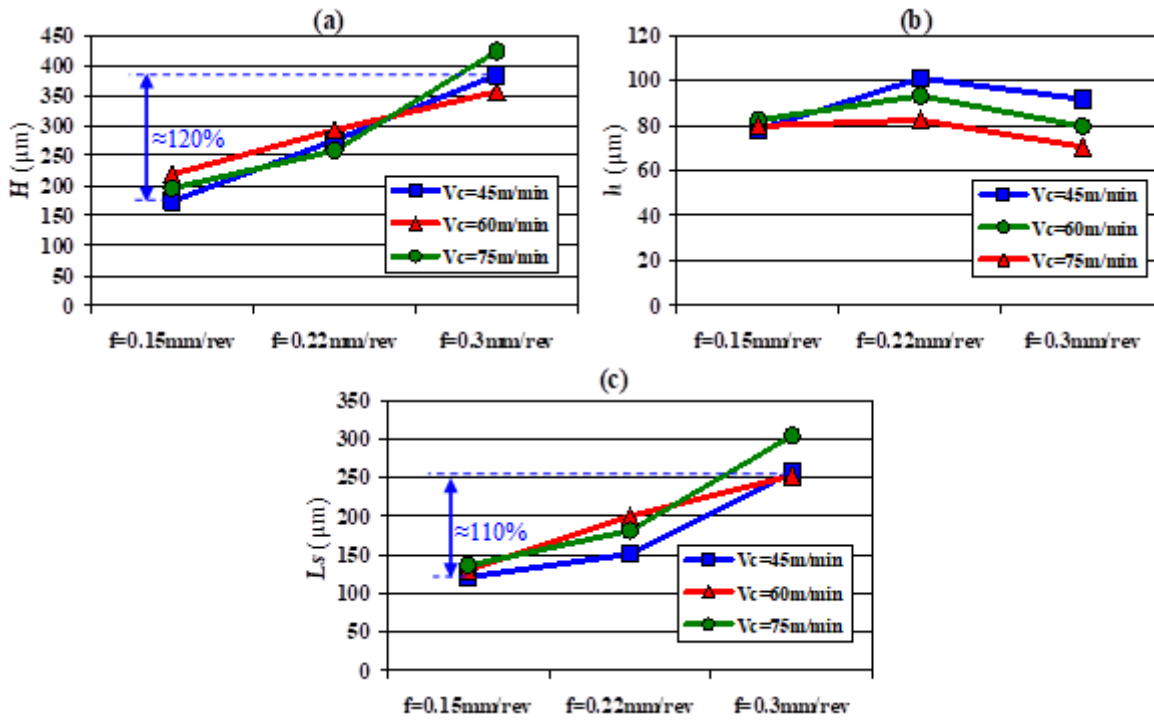


Figure 14

Experimental average (a) peak height, (b) valley height and (c) segments width for different cutting conditions

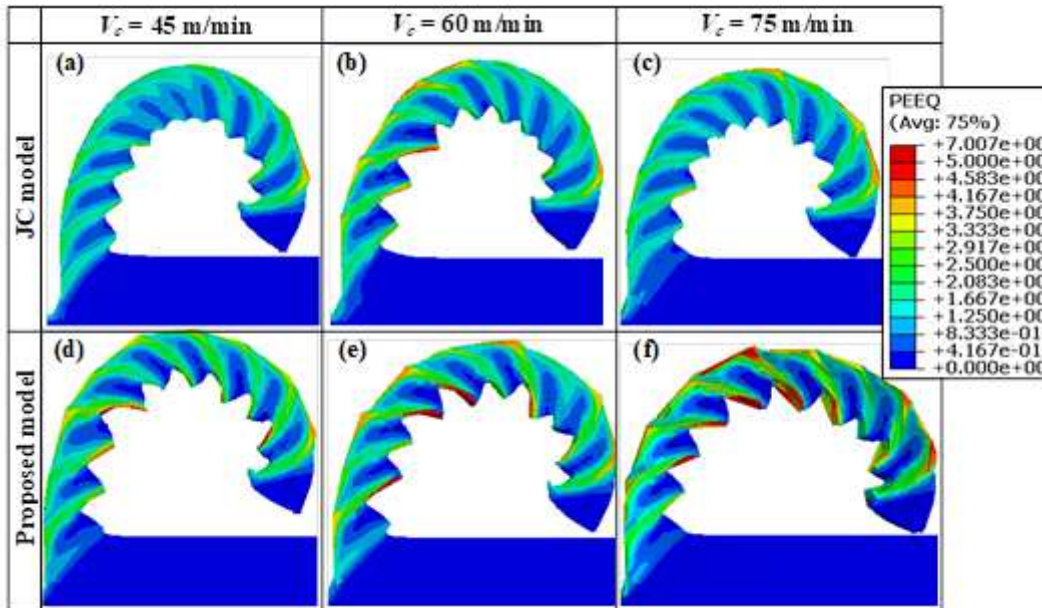


Figure 15

Numerical chip morphology predicted with (a-c) the JC and (d-f) the proposed rheological models and corresponding to different cutting speeds ($f = 0.15$ mm/rev)

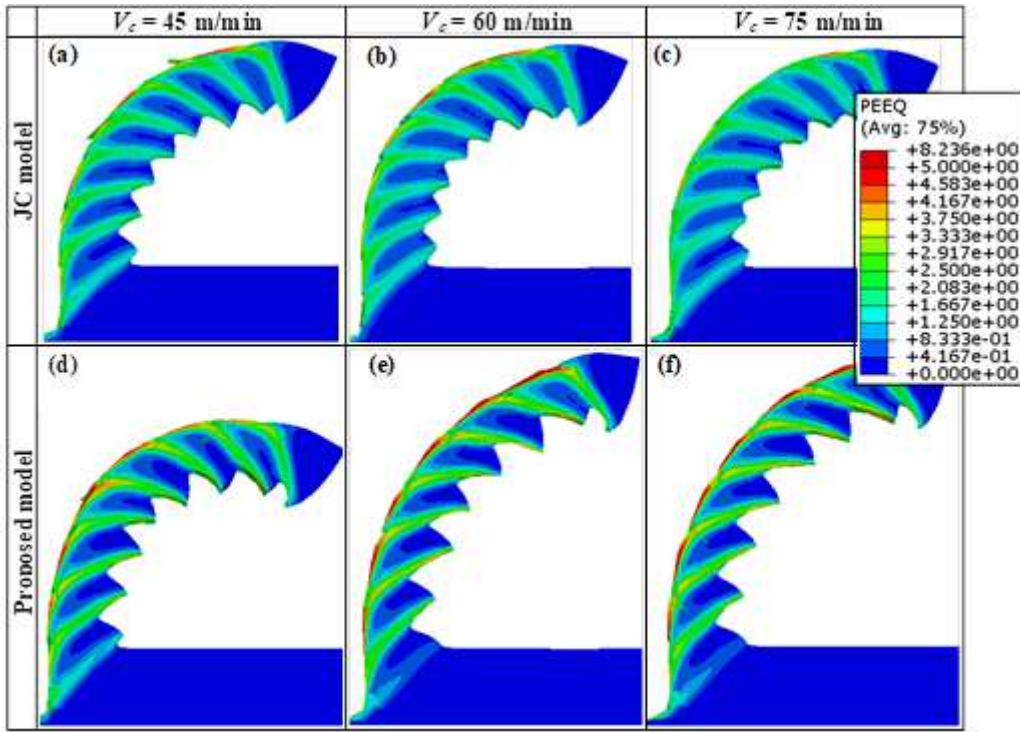


Figure 16

Numerical chip morphology modeled with different rheological models for several cutting speeds ($f = 0.22 \text{ mm/rev}$)

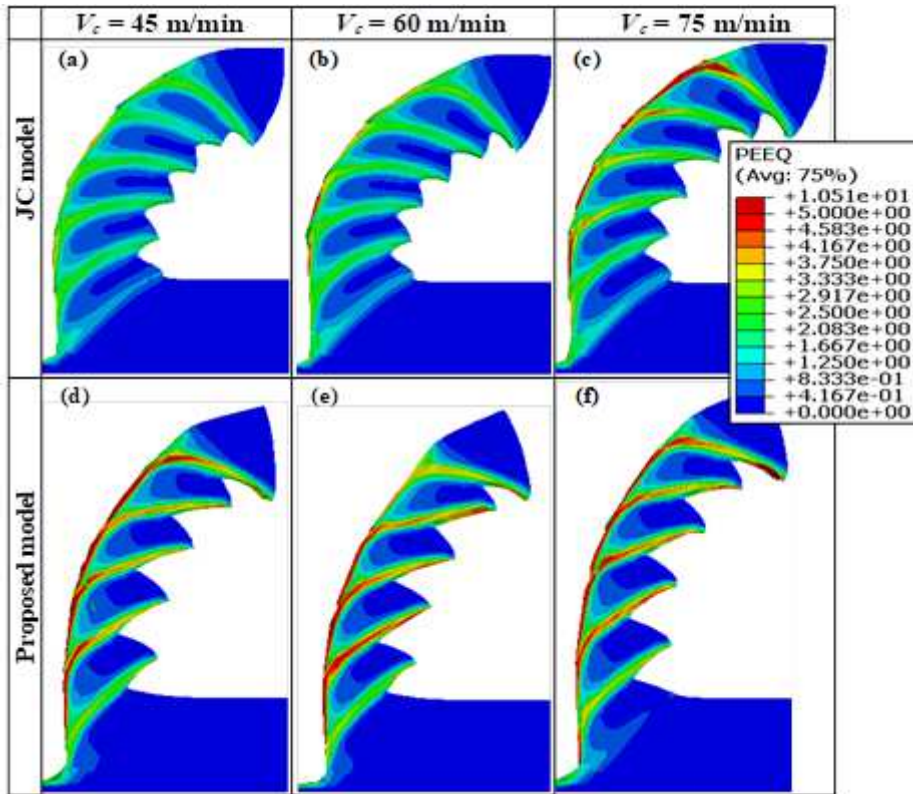


Figure 17

Numerical chip morphology for a feed rate of 0.3 mm/rev and different cutting speeds: (a-c) JC and (d-f) proposed rheological models

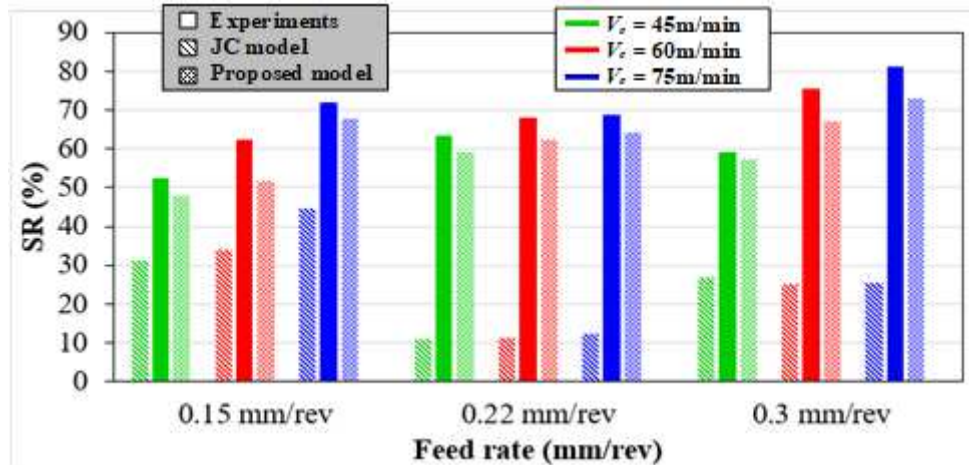


Figure 18

Comparison of experimental and numerical segmentation ratio for different cutting conditions

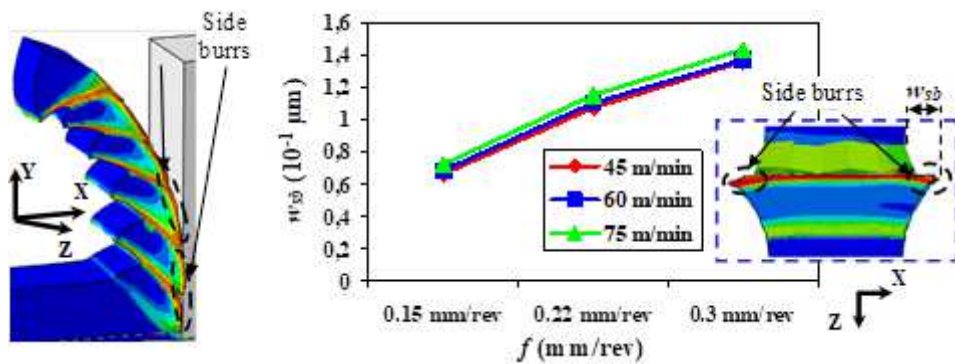


Figure 19

Side burrs width corresponding to different cutting conditions

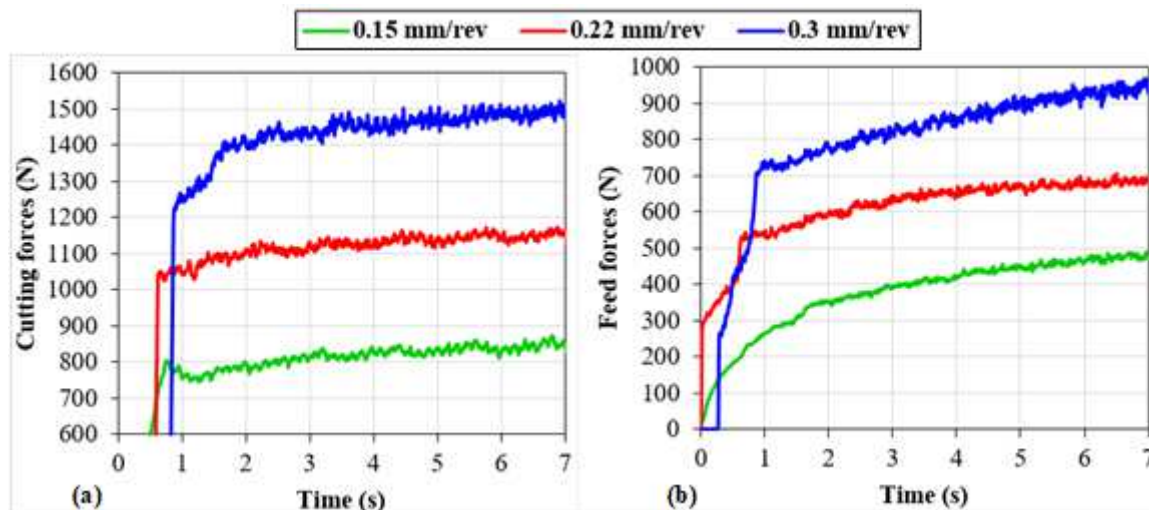


Figure 20

Experimental forces corresponding to different feed rates ($V_c = 45$ m/min): (a) cutting and (b) feed forces

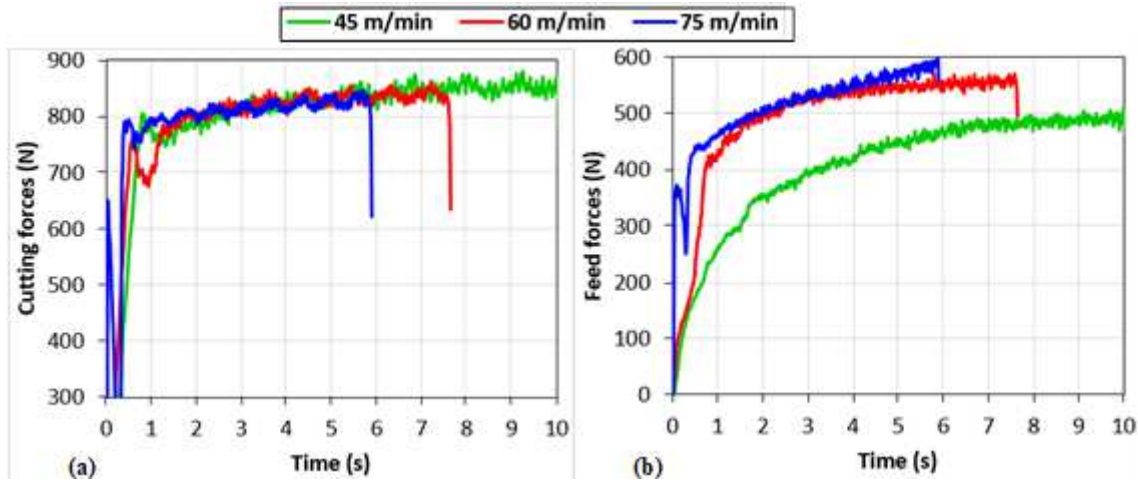


Figure 21

Experimental (a) cutting and (b) feed forces obtained for different cutting speeds ($f = 0.15$ mm/rev)

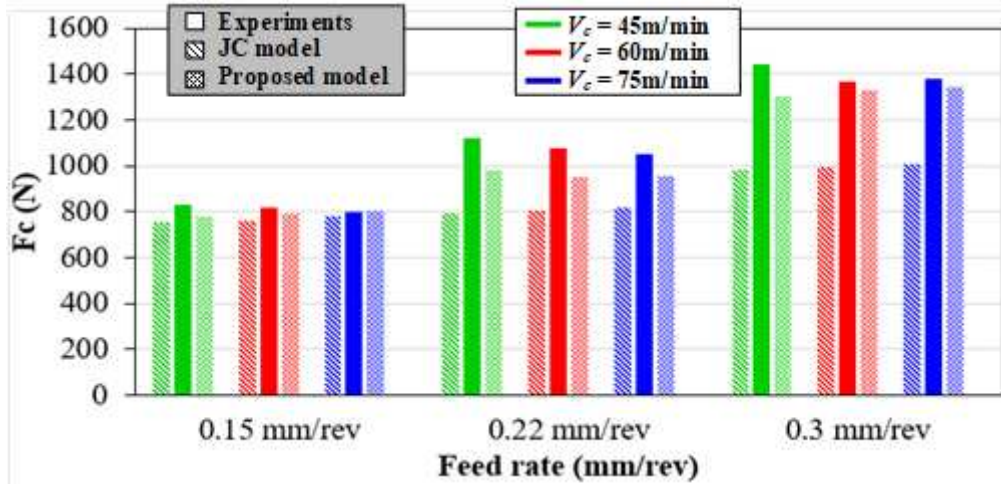


Figure 22

Mean experimental and numerical cutting forces corresponding to different cutting conditions